CHALMERS
UNIVERSITY OF TECHNOLOGY

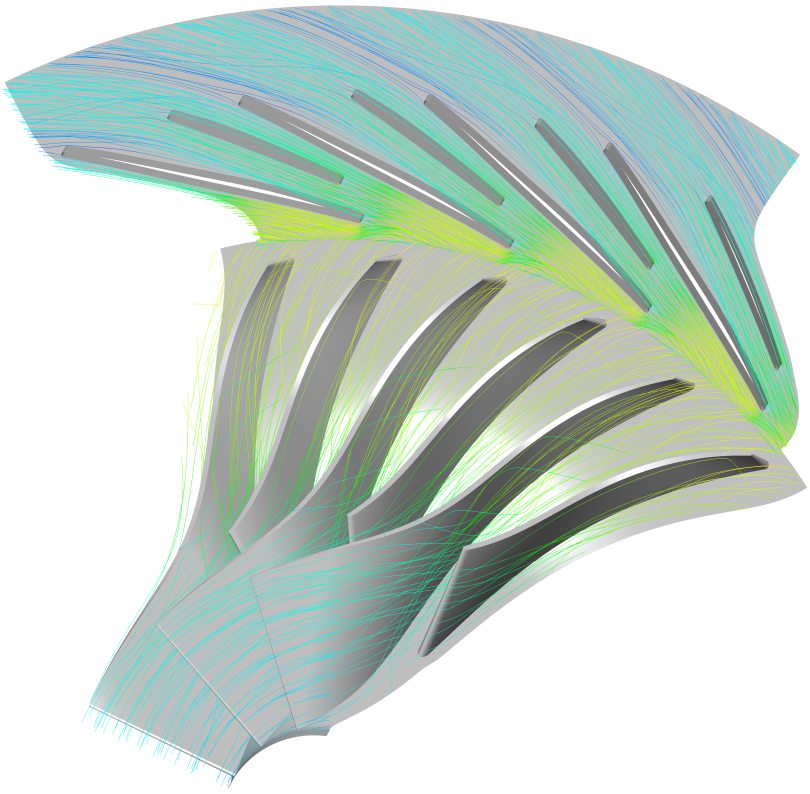

Numerical Study on Centrifugal Compressors for Small Aero Engines

Validation of a Radial Impeller and Diffuser Design for Minimal Frontal Area

Master's thesis in Mobility Engineering

OLIVER SANDBERG

DEPARTMENT OF MECHANICS AND MARITIME SCIENCES
CHALMERS UNIVERSITY OF TECHNOLOGY
Gothenburg, Sweden 2026
www.chalmers.se

Master's Thesis in Mobility Engineering

Numerical Study on Centrifugal Compressors for Small Aero Engines

Validation of a Radial Impeller and Diffuser Design for Minimal Frontal Area

OLIVER SANDBERG

CHALMERS
UNIVERSITY OF TECHNOLOGY

Department of Mechanics and Maritime Sciences
Division of Fluid Dynamics
Chalmers University of Technology
Gothenburg, Sweden 2026

Numerical Study on Centrifugal Compressors for Small Aero Engine
Validation of a Radial Impeller and Diffuser Design for Minimal Frontal Area
OLIVER SANDBERG

Supervisor: Dr. Debarshee Ghosh, GKN Aerospace
Examiner: Prof. Tomas Grönstedt, Department of Mechanics and Maritime Sciences

Master's Thesis 2026
Department of Mechanics and Maritime Sciences
Chalmers University of Technology
SE-412 96 Gothenburg
Sweden
Telephone +46 31 772 1000

Cover: Three dimensional streamlines of the absolute velocity through a centrifugal impeller and radial vaned diffuser.

Typeset in LaTeX
Gothenburg, Sweden 2026

Numerical Study of Centrifugal Compressors in Small Aero Engines
A study of diffuser design for minimal frontal area for small aero engines
OLIVER SANDBERG
Department of Mechanics and Maritime Sciences
Division of Fluid Dynamics
Chalmers University of Technology

Abstract

Most modern aircraft engines employ multistage axial compressor configurations. However, in small aero engines, axial compressors face substantial challenges. As mass flow is conserved, blade height decreases with each stage, and in small compressors this reduction becomes significant due to end wall boundary layer growth, large tip gap ratios, and pronounced secondary flow effects. An alternative is the use of an axi-centrifugal compressor configuration, where the high pressure axial stages are replaced by a centrifugal compressor. While centrifugal compressors provide higher pressure ratios within a shorter axial length, they introduce challenges related to engine frontal area. The frontal area scales with the compressor pressure ratio and is constrained by the overall engine geometry. The objective of this thesis is to numerically investigate centrifugal compressor design concepts aimed at achieving high aerodynamic performance within a confined space. The NASA High Efficiency Centrifugal Compressor impeller is replicated and validated. Subsequently, four diffuser designs are developed and evaluated using Computational Fluid Dynamics. Vaned diffusers are analysed and compared using standard performance parameters, and the influence of splitter vanes is examined. The results indicate more stable performance for the wedge diffuser compared to the cascade design. Splitter vanes extend and stabilize the operating range of both designs, but at the cost of increased total pressure losses. Due to wake-related issues in the wedge diffuser, the cascade combined with splitter vanes is found to be beneficial. While the goal of achieving significantly higher performance is only partially met, the study provides valuable insights into diffuser design trade-offs for small aero engine applications.

Keywords: Centrifugal Compressor, Centrifugal Diffuser, Splitter Vanes, Pressure Recovery, Aerodynamic Performance

Preface

This report presents the outcome of my master's thesis project carried out at GKN Aerospace Sweden AB in collaboration with the Department of Mechanics and Maritime Sciences at Chalmers Univeristy of Technology during the spring of 2026. The work focuses on the aerodynamic design and analysis of centrifugal compressor diffusers using Computational Fluid Dynamics. It aims to contribute to the understanding of performance and stability characteristics of diffuser concepts for small aero-engine applications. Finally, this concludes my five years of engineering studies.

Acknowledgements

I would like to express my sincere gratitude to my supervisor Dr. Debarshee Ghosh at GKN Aerospace Sweden for valuable guidance, insightful discussions, and continuous support throughout this thesis. I also wish to thank GKN Aerospace Sweden for providing the opportunity to carry out this project in the first place, and especially the Future Concepts team for a fun time in a new and unknown enviroment. I am grateful to my fellow master thesis colleagues in close quarters for both fun chats and insightful discussions. Not to be forgotten are also all my teachers at Chalmers University of Technology throughout the years. Lastly my family for their encouragement and support during the course of this spring and all these years, especially my beloved Rebecca.

Oliver Sandberg, Gothenburg, May 2026

List of Acronyms

Below is the list of acronyms that have been used throughout this thesis listed in alphabetical order:

2D	Two Dimensional
ADP	Aerodynamic Design Point
CFD	Computational Fluid Dynamics
CD	Cascade Diffuser
CSD	Cascade Splitter Diffuser
HECC	High Efficiency Centrifugal Compressor
HPC	High Pressure Compressor
LE	Leading Edge
OGV	Outlet Guide Vane
PRTT	Total-to-Total Pressure Ratio
RANS	Reynolds Average Navier Stokes
SST	Shear Stress Transport
TE	Trailing Edge
VLD	Vaneless Diffuser
WD	Wedge Diffuser
WSD	Wedge Splitter Diffuser

Nomenclature

Below is the nomenclature of characters, subscripts and non-dimensional numbers that have been regulary used throughout this thesis.

Latin Characters Variables

A	Area [m^2]
b	Blade or Vane Height [m]
$\vec{c}$ or c	Absolute Velocity [m/s]
h	Specific Enthalpy [J/kg]
l	Chord Length [m]
L	Length [m]
$\dot{m}$	Mass Flow [kg/s]
p	Pressure [Pa]
R or r	Radius [m]
s	Tip Gap Length [m]
T	Temperature [K]
$\vec{U}$ or U	Blade Speed [m/s]
W	Width [m]
$\vec{w}$ or w	Relative Velocity [m/s]

Greek Characters Variables

α	Absolute Flow/Swirl Angle [°]
β	Relative Flow Angle or Blade Metal Angle [°]
ω	Rotational Speed [rad/s]
θ	Circumferential Position or Half Angle [rad]
ρ	Density [kg/m^3]

Subscripts

0	Total Properties
1	Station at Impeller Entry
2	Station at Impeller Exit
3	Station at Diffuser Entry
4	Station Diffuser Exit
ax	Axial Components
d	Diffuser
h	Hub
i	Impeller
is	Isentropic
m	Meridional Components
r	Radial Components
s	Shroud
tip	Blade Tip
$u2$	Impeller Blade Exit
θ	Circumferential Components

Non-Dimensional Numbers

AR	Area Ratio
C_P	Static Pressure Recovery Coefficient
DF	Lieblein Diffusion Factor
DH	de Haller Number
L/W	Length over Width Ratio
M	Mach Number
Re	Reynolds Number
Z	Number of Blades/Vanes
γ	Ratio of Specific Heats
ϕ	Flow Coefficient
σ	Solidity
λ	Work Coefficient
ζ	Total Pressure Loss Coefficient

ξ	Kinetic Energy Recovery Coefficient

Contents

List of Figures

List of Tables

1

Introduction

This chapter provides a brief introduction to gas turbines, aero-engines, and outlines the scope of this thesis work.

1.1 Background

A typical gas turbine consists of four aerodynamic components: a compressor, a combustor, a turbine and a nozzle. The thermodynamic principle of a gas turbine is the Brayton cycle [1] illustrated by the Temperature-entropy ($T - s$) diagram in Fig. 1.1.

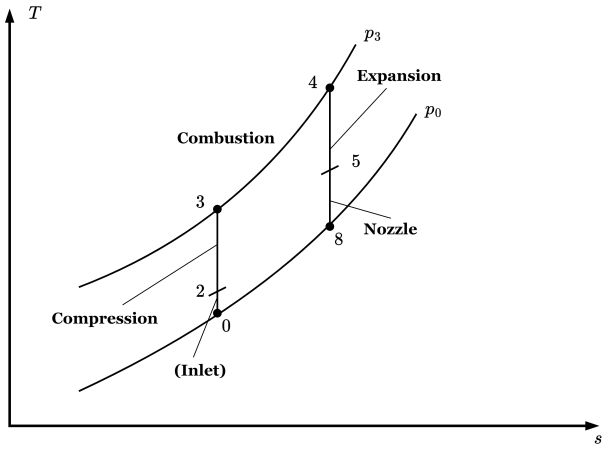

Figure 1.1: The ideal Brayton Cycle illustrated in a $T - s$ diagram.

The Brayton cycle describes the change of the state variables pressure (p), temperature (T) and entropy (s), as the gas flows through the gas turbine. A gas turbine ingests gas (0-2, Fig. 1.1), usually air, and compresses it by performing work on the fluid resulting in an increase in the total (p_0) and static pressure, total (T_0) and static temperature, of the flow, as illustrated by the vertical line 2-3 in Fig. 1.1. The compression process is considered to be isentropic ($\Delta s = 0$), i.e., reversible and adiabatic.

The compressed gas is mixed with fuel and burned in the combustor, adding heat to the flow and consequently increasing the temperature and entropy of the flow, as

indicated by line 3-4 in Fig. 1.1. The hot compressed gas then flows through the turbine where work is done by the gas on the rotating turbine blade rows, which drive the shaft that is connected to the compressor (4-5, Fig. 1.1). Typically, the low-pressure turbine shaft powers the low pressure compressor and the fan, and the high pressure turbine shaft powers the High Pressure Compressor (HPC). Finally, the nozzle expands the flow back to atmospheric pressure and exhausts it at a high velocity to generate forward thrust (5-8, Fig. 1.1).

The compressor is a power consuming turbomachine. It performs work on the gas, flowing through rotating blade rows which results in an increase in the total enthalpy (h_0), total pressure and total temperature of the flow. Compressors can be classified by the direction of flow at the exit of the rotor into axial, radial and mixed flow compressors. In an axial compressor the flow at the exit of the rotor is primarily parallel to the rotational axis, in a radial compressor the flow exiting the rotor is primarily perpendicular to the rotational axis. A schematic of the flow direction in the different types of compressors is illustrated in Fig. 1.2. Based on the operation regime, compressors are classified as either compressible or incompressible machines. A compressor is considered to be operating in the incompressible flow regime, if the Mach number (M) is below 0.3, and the density change ($\Delta\rho/\rho$) is below 5% everywhere within the turbomachine. The focus of this thesis is compressible radial compressors [2].

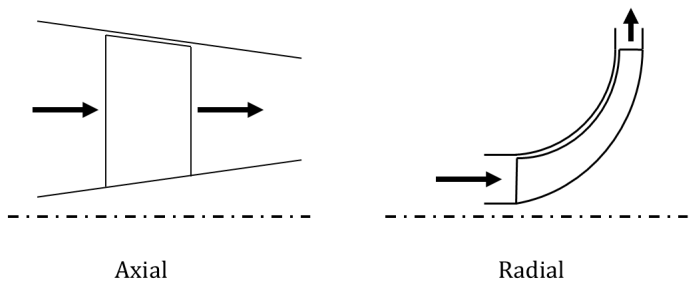

Figure 1.2: Flow direction of different compressors.

Most modern day civil and military aircrafts use multistage stage axial compressors. This type of turbomachine are a suitable for large aircraft engines but they are vulnerable in smaller engines. In an axial compressor, the annular flow area decreases progressively for every successive stage as the fluid density increases. This reduction in annular area results in a corresponding reduction in blade height. Consequently, in the rear stages of a HPC, the blade aspect ratio, the ratio of blade chord (l) over blade height (b), decreases.

These limitations are particularly severe in small engine applications, where constraints on overall engine size further restrict the minimum attainable blade height for the last stages of the HPC. As the blade height is reduced, end-wall boundary layers and tip leakage flow occupy an increasingly larger fraction of the blade height, leading to increased losses, reduced efficiency, and diminished stall margin. Ultimately, when the blade height becomes sufficiently small, end-wall effects dominate the flow field, rendering axial compressor stages inefficient for the final stages

of the HPC in small engines [2].

These limitations motivates the choice to use centrifugal compressors as the HPC for small engine applications. A centrifugal compressor allows for increased pressure ratio in the available axial space compared to axial compressors. A centrifugal compressor performs work on the flow by turning the flow in the circumferential direction (imparting swirl to the flow), and by increasing the radius of the flow from the inlet to the outlet (centrifugal effect), i.e., the radius of the streamline increases from the rotor inlet to the outlet. In comparison, an axial compressor performs work on the flow, only through flow turning. However, there is a limitation to the amount of flow turning that can be achieved before flow separation occurs on the blade surface. Therefore, a centrifugal compressor can achieve a higher total pressure ratio per stage compared to an axial compressor. Pressure ratios of 8:1 have been achieved for a single centrifugal stage [2].

Small aero engines are used in helicopters, unmanned aerial vehicles, auxiliary power units and in smaller business jets where there are significant dimensional constraints [3]. Centrifugal compressors in jet engine applications are typically used as the HPC in an axi-centrifugal compressor. An example of this is illustrated in Fig. 1.3 of the Honda HF-120 engine, where the difference between a centrifugal impeller and an axial blade row is also illustrated.

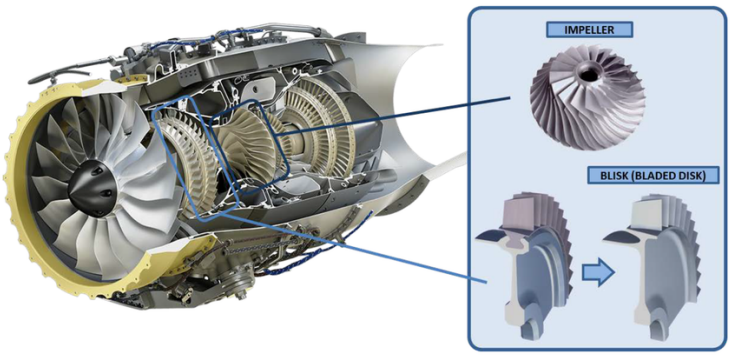

Figure 1.3: Cut-away of the Honda HF-120 engine, reproduced with permission [4].

A centrifugal stage for an aero engine has four components; a rotating impeller, a radial diffuser, a radial-to-axial bend and an axial Outlet Guide Vane (OGV). In Fig. 1.4 a schematic view of the components is shown.

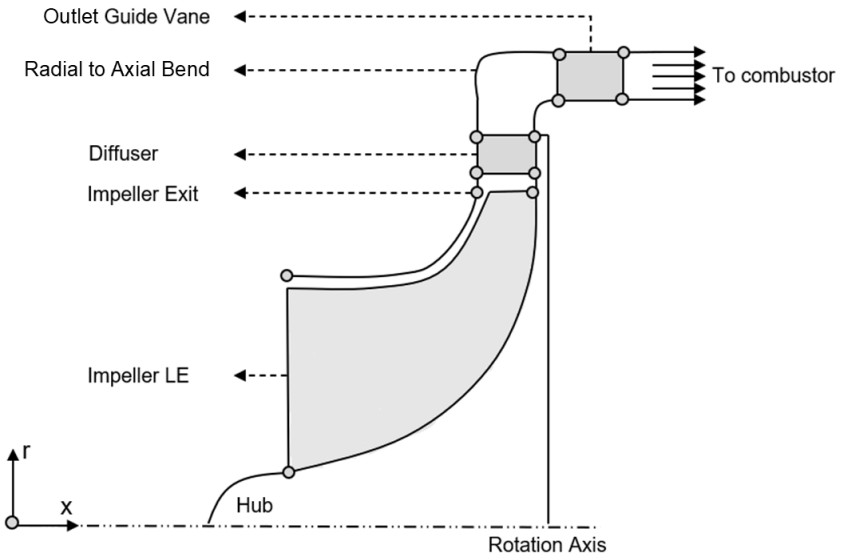

Figure 1.4: Schematic view of a centrifugal compressor.

Centrifugal compressors used in small engine applications present significant design challenges, with the main issue being the increase in engine frontal area compared to an equivalent axial stage. The frontal area is largely determined by the pressure ratio requirement. The achievable pressure rise in a centrifugal compressor is proportional to the square of the impeller tip speed ($\Delta H \propto U_2^2$). However, rotational speed (ω) is often limited by mechanical stresses and material constraints. As a result, higher pressure ratios require an increase in the impeller exit radius (R_2). An increase in impeller exit radius leads to higher flow velocities at the impeller exit. The flow exiting the impeller must then be diffused to meet combustor inlet requirements.

Therefore, the high-kinetic energy flow exiting the impeller must be diffused efficiently to recover the static pressure without excessive total pressure losses. To achieve this, radial diffusers with large exit radii are ideally required. This creates a compounding effect, i.e., a high total pressure ratio requirement requires an impeller with high exit radius. A larger impeller in turn requires a larger diffuser to meet the inlet condition requirements for the combustion chamber. A larger diffuser increases the overall casing size. This overall increase in the radius of the stage leads directly to an increase in engine frontal area, which in turn results in a heavier engine with higher aerodynamic drag and increased fuel consumption.

This problem is more severe in small engines. The available radial and axial space is limited, i.e., the required diffusion must be achieved in very limited radial and axial space. Typically, for engines with a centrifugal stage, the maximum diameter of the engine and subsequentially the engine frontal area, is determined by the diameter of the centrifugal compressor.

One concept that has addressed these challenges is the High Efficiency Centrifugal Compressor (HECC) from NASA [5], which is a small centrifugal compressor for rotorcraft applications. This compressor addresses the full envelope of challenges connected to centrifugal compressors in small engine concepts.

1.2 Objective

The main challenge related to centrifugal compressor in small engine applications is to minimize the total frontal area by reducing the radial extent of the centrifugal compressor. The radial extent of a centrifugal stage is determined by the below four geometric dimensions:

1. The impeller exit radius. As mentioned previously the impeller exit radius is often determined by the required pressure ratio and rotational speed of the shaft.

2. The radial gap between the impeller and the radial diffuser

3. The radial extent of the radial vaned diffuser

4. The radial-to-axial bend.

This thesis work, will focus on investigation the radial gap between the impeller and diffuser, and the radial extent of the radial diffuser.

1.2.1 Research Questions

- Which design parameters influence the pressure recovery and range of a radial vaned diffuser stage?
- How can these parameters be modified to reduce the radial extent while maintaining diffuser performance or keep the radial extent while improving the diffuser performance?

1.2.2 Limitations

No physical experiments are performed in this thesis; all results are obtained through Computational Fluid Dynamics (CFD) simulations. The impeller geometry is fixed, no optimisation of the impeller is considered. Additionally, the radial-to-axial bend and the OGV are not included in the simulations.

2

Theory

This chapter presents the theory associated with this thesis. It provides an overview of the aerodynamics of centrifugal compressors. The key performance parameters used to evaluate compressor behaviour are clearly defined. In addition, a review of the Computational Fluid Dynamics (CFD) methods relevant to this work is included.

2.1 Overview of Centrifugal Compressors

The Aerodynamic Design Point (ADP) of a compressor or fan is defined by its rotational speed (n [RPM]) and the ingested mass flow rate ($\dot{m}$). At a specified ADP, the aerodynamic performance is quantified by the total-to-total pressure ratio (PRTT) and isentropic efficiency (η_{is}). The performance over the operating range of a compressor is commonly illustrated by a compressor map, as seen in Fig. 2.1 where the PRTT is plotted as function of massflow.

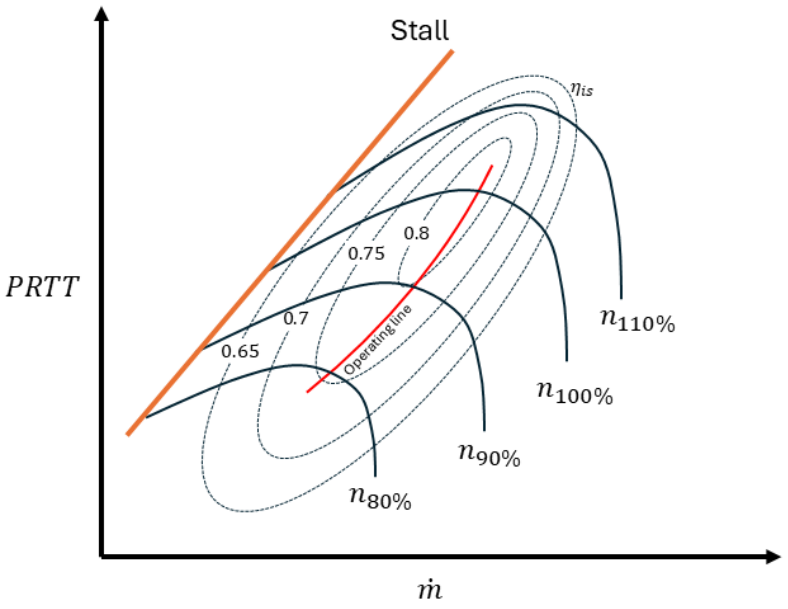

Figure 2.1: Schematic of a compressor map with stall line, speedlines and isentropic efficiency contours.

The isentropic efficiency is defined in Eq. 2.1, where π is the total pressure ratio and τ is the total temperature ratio.

$$\eta_{is} = \frac{\pi^{(\gamma-1)/\gamma} - 1}{\tau - 1} \tag{2.1}$$

The total-to-total pressure rise of a centrifugal stage is determined from the mass-flow-averaged total pressure at the inlet and outlet of the machine. In a complete centrifugal stage, this corresponds to the impeller inlet (station 1) and the OGV exit (station 6), as illustrated in Fig. 2.2. In the present work, only the impeller and the radial vaned diffuser are modelled in to numerical domain, and therefore the performance is evaluated between station 1 and station 4.

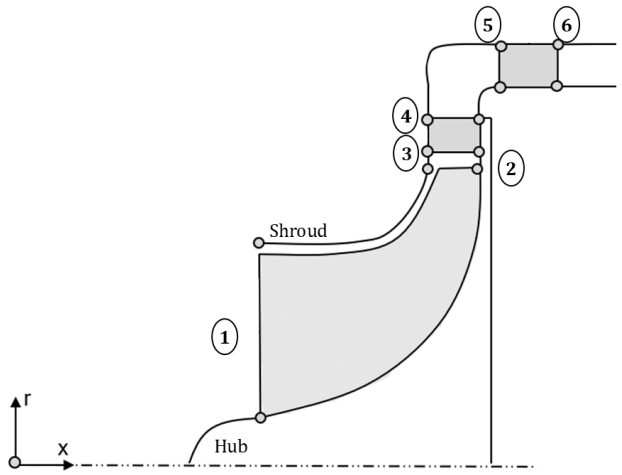

Figure 2.2: Schematic of a centrifugal compressor stage with station numbering.

The total-to-total efficiency is defined as the ratio between the ideal isentropic work and the actual work input. The shaft power required to drive the compressor is calculated as the product of the shaft rotational speed (ω [-/s]) and the applied torque ($\omega \cdot T$). To enable comparison between different machines and operating conditions, non-dimensional parameters are commonly used. The most relevant parameters for a centrifugal compressor are the global flow coefficient (ϕ) and the work coefficient (λ), defined in Eq. 2.2 and Eq. 2.3 respectively, where $A_2 = D_2^2$ and $U_2 = \omega R_2$. The operating regime of the compressor is further characterised using the Mach number (M, Eq. 2.4) and Reynolds number (Re, Eq. 2.5) where u is the fluid velocity and μ the dynamic viscosity.

$$\phi = \dot{m}/(\rho_{01} A_2 U_2) \tag{2.2}$$

$$\lambda = \Delta h_0 / U_2^2 \tag{2.3}$$

$$M = \frac{u}{a} \tag{2.4}$$

$$Re = \frac{\mu u L}{\rho} \tag{2.5}$$

The schematic for a centrifugal compressor stage with key geometric parameters marking the radial and axial extent of the different components of a centrifugal stage is illustrated schematically in Fig. 2.3. These include the impeller inlet hub and shroud radii (R_{h1} and R_{s1}) at the Leading Edge (LE), the impeller exit radius (R_2) at the Trailing Edge (TE), the diffuser inlet and outlet radii (R_3 and R_4), and the maximum stage radius (R_{max}). Additional geometric parameters include the impeller exit width (b_2), the axial length of the impeller (L), and the tip clearance (s_{tip}).

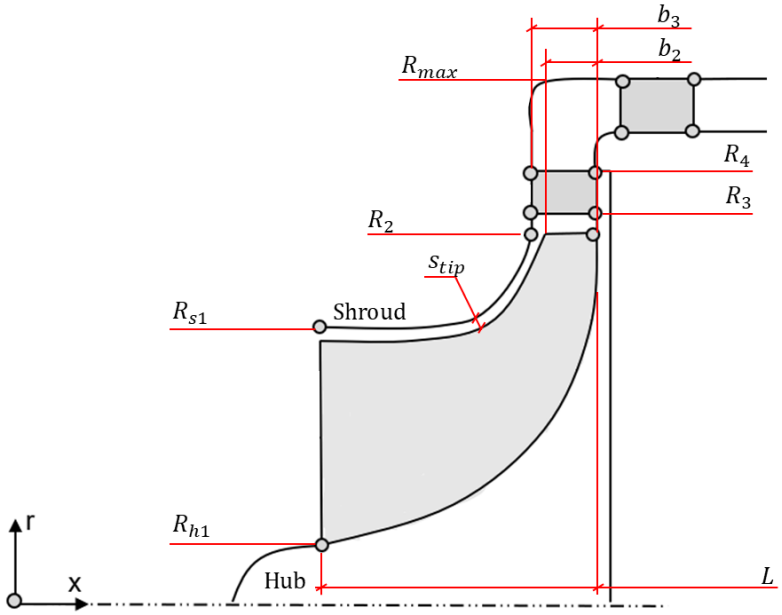

Figure 2.3: Schematic of a centrifugal compressor stage important geometric measurements.

At any operating point, the flow through the centrifugal impeller is typically described using velocity triangles at the inlet and outlet, as shown in Fig. 2.4. Absolute velocities ($\vec{c}$) and flow angles (α) are defined in the stationary frame of reference, while relative velocities ($\vec{w}$) and flow angles (β) are defined in the rotating frame. Subscripts 1 and 2 denote impeller inlet and outlet conditions of the impeller, respectively. The absolute velocity is given by the vector sum of the blade velocity ($\vec{U}$) and the relative velocity as defined in Eq. 2.6.

$$\vec{c} = \vec{U} + \vec{w} \tag{2.6}$$

Both absolute and relative velocities can be decomposed into axial, radial, and circumferential components. The vector sum of axial and radial components define the meridional velocity component, given by Eq. 2.7.

$$c_m^2 = c_{ax}^2 + c_r^2 \tag{2.7}$$

For centrifugal compressors, the inlet flow is often assumed to be purely axial, such that $c_{r1} = c_{\theta 1} = 0$. The blade speed is defined as $U = \omega r$, and increases from inlet to outlet due to the increase in radius ($U_2 > U_1$).

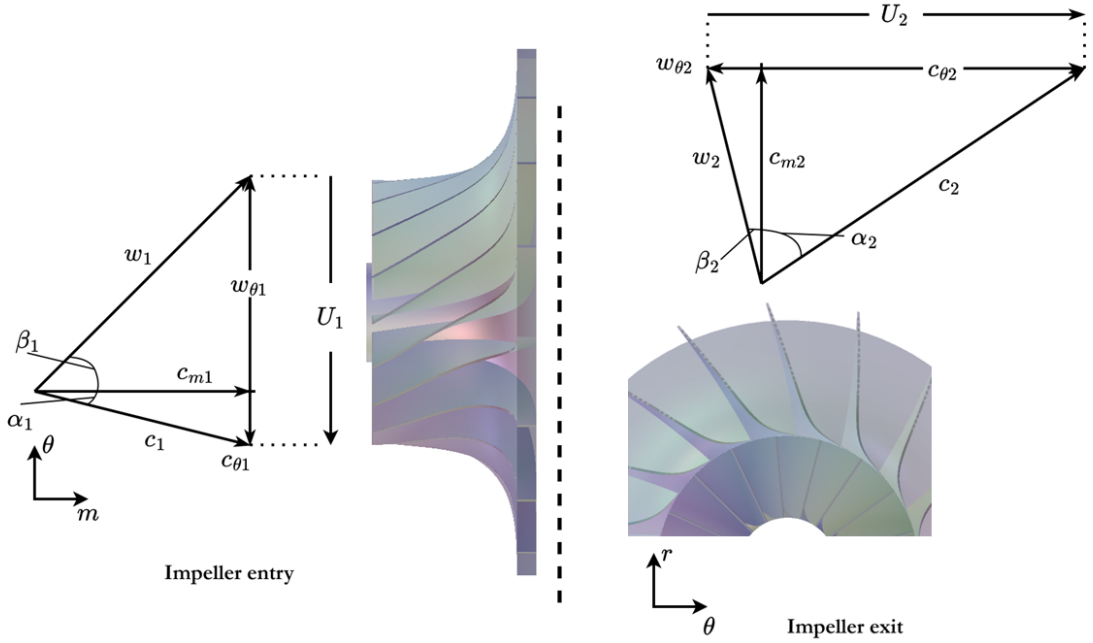

Figure 2.4: Velocity triangles of a centrifugal compressor impeller [2].

The flow enters with an absolute flow velocity, c_1, with swirl angle, α_1. The rotor is met in the relative frame by the relative velocity, w_1, with flow angle, β_1. U_1 is the blade speed at the mean inlet radius. With this, the trigonometric relations for the circumferential velocities can be determined according to Eq. 2.8a–2.8c.

$$c_{\theta 1} = c_1 \sin \alpha_1 = c_{m1} \tan \alpha_1 \tag{2.8a}$$

$$w_{\theta 1} = w_1 \sin \beta_1 = c_{m1} \tan \beta_1 \tag{2.8b}$$

$$U_1 = c_{\theta 1} + w_{\theta 1} \tag{2.8c}$$

As the flow passes through the impeller, it is turned in the circumferential direction, increasing the circumferential component of the absolute velocity ($c_{\theta 2} > c_{\theta 1}$), i.e., the rotor imparts swirl to the flow ($\alpha_2 > \alpha_1$). Simultaneously, the relative velocity and relative flow angle decreases ($w_2 < w_1$) and ($\beta_2 < \beta_1$) due to diffusion within the blade passage.

With the velocities from the velocity diagrams in Fig. 2.4, the specific work (ΔW) can be defined with the Euler work equation, in Eq. 2.9.

$$\Delta W = \Delta h_0 = U_2 c_{\theta 2} - U_1 c_{\theta 1} \tag{2.9}$$

In the absence of inlet swirl ($c_{\theta 1} = 0$), the work input is primarily governed by the impeller exit conditions, indicating that higher blade speed and greater circumferential velocity at the outlet lead to increased energy transfer to the flow. The Euler work equation can also be interpred by the following derivation, beginning with substituting $c_\theta = U + w_\theta$ in Eq. 2.9.

$$\begin{aligned}
\Delta W &= U_2 \left(U_2 + w_{\theta 2}\right) - U_1 \left(U_1 + w_{\theta 1}\right) \\
&= \left(U_2 w_{\theta 2} - U_1 w_{\theta 1}\right) + \left(U_2^2 - U_1^2\right) \\
&= U_2 \left(w_{\theta 2} - \frac{U_1}{U_2} w_{\theta 1}\right) + U_2^2 \left(1 - \frac{U_1^2}{U_2^2}\right)
\end{aligned}$$

Substituing U_1 and U_2 in the parentheses with $U = \omega r$ the final equation yields as Eq. 2.10.

$$\Delta W = \underbrace{U_2 \left(w_{\theta 2} - \frac{R_1}{R_2} w_{\theta 1}\right)}_{Term\ 1} + \underbrace{U_2^2 \left(1 - \frac{R_1^2}{R_2^2}\right)}_{Term\ 2} \tag{2.10}$$

Term 1 is the turning term, while Term 2 is the centrifugal term. The turning term is the work done due to the turning of the flow in the circumferential direction by the rotor blades. The centrifugal term is the work done as a result of the centrifugal effect, i.e., changing the radius of the flow. For an axial machine there is no change in the radius of the streamlines, i.e., $R_1 = R_2$. It follows that there is no centrifugal effect for axial machines. And all work for an axial machine is achieved through flow turning. Similarly it follows that the larger the change of radius in a centrifugal compressors, larger the work done and therefore higher the achievable pressure ratio. A higher radius also implies a higher blade tip speed (U_2), which then according to Eq. 2.8c implies a higher exit circumferential velocity and higher exit swirl angle. Therefore it follows, that for impellers with high pressure ratios, the exit swirl angle is high, which leads to the need for a vaned diffuser.

2.1.1 Impeller Outflow and Tip Leakage

The flow leaving the impeller has high absolute velocity and high swirl [6]. Experiments show that the impeller exit flow is highly non-uniform and rotating. A common model for describing this behaviour is the jet-wake theory [7], which divides the impeller outflow into a high-velocity jet on the pressure side and a low-velocity wake on the suction side, producing circumferential velocity variations. This model

is based on simplified assumptions such as two-dimensional (2D), incompressible, steady flow with constant exit angle β_2. In reality, the impeller discharge flow is more complex. The velocity profile varies both circumferentially and in the axial (hub-shroud) direction [6], as illustrated in Fig. 2.5.

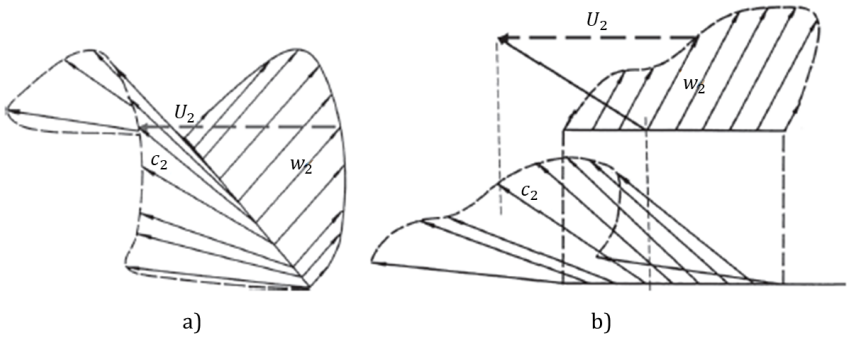

Figure 2.5: Axial a), and cirumferential b) velocity distortion from the impeller, adapted from [8].

Recent studies shows that the wake structure is not of a simple 2D structure but three-dimensional [9]. A low-momentum region typically forms near the shroud due to secondary flows driven by tip leakage through the clearance between the blade tip and shroud as illustrated in Fig. 2.6 [9]. There is also a larger wake region referred to as channel wake in Fig. 2.6 and a blade wake, with only a small jet region near the pressure side of the blade. The tip flow has high vorticity and persist when flowing downstream from impeller while the jet, blade-wake and parts of the channel wake mix out downstream of the impeller TE.

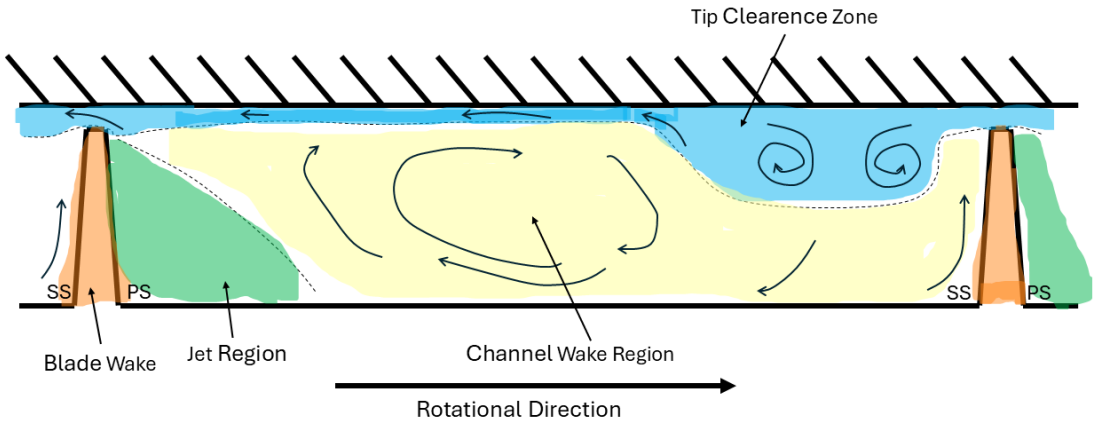

Figure 2.6: The complex outflow structure at the impeller exit (radial velocity component), consisting of tip flow, blade wake flow, channel wake flow and a small jet stream, adapted from [9].

2.2 Radial Diffusers

Diffusers for centrifugal compressors maybe either vaned or vaneless. The choice between the two is dependent on the exit swirl angle from the impeller and the radial space available to de-swirl the flow. The role of the diffuser is to convert the kinetic energy of the air imposed by the impeller into static pressure rise. The meridional velocity and the circumferential velocity decreases with increase in radius. Figure 2.7 shows the nomenclature for a vaned diffuser. The same station numbering is applicable for the vaneless context.

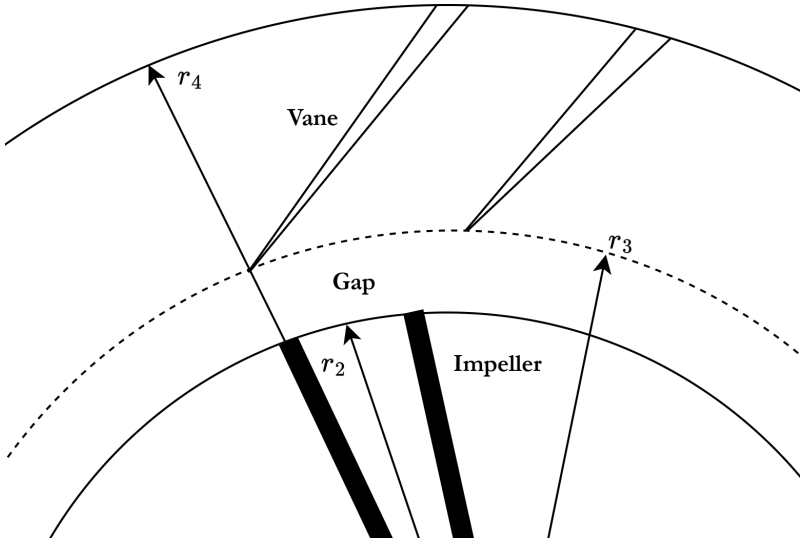

Figure 2.7: Station numbering of a diffuser.

2.2.1 Vaneless Diffusers

The vaneless diffuser is a geometrically simple component [10]. It consists of an annular channel with an increasing flow area in the radial direction. From the continuity equation, a relationship between the inlet and outlet flow properties can be established [8], as given by Eq. 2.11, where index 3 denotes the diffuser inlet and index 4 the diffuser outlet.

$$\rho_3 c_{m3} b_3 2\pi r_3 = \rho_4 c_{m4} b_4 2\pi r_4 \tag{2.11}$$

For a diffuser of constant width ($b_2 = b_3$) and assuming incompressible flow through the diffusers ($\rho_3 = \rho_4$), Eq. 2.11 simplifies to Eq. 2.12

$$c_{m3} r_3 = c_{m4} r_4 \tag{2.12}$$

From Eq. 2.12, it follows that since $r_3 < r_4$, the meridional velocity decreases across the diffuser, i.e., $c_{m4} < c_{m3}$. A similar relation can be obtained from the conservation

of angular momentum, given by Eq. 2.13

$$c_{\theta 3} r_3 = c_{\theta 4} r_4 \tag{2.13}$$

From Eq. 2.13, it can be seen that the circumferential velocity also decreases with increasing radius ($c_{\theta 4} < c_{\theta 3}$).

Consequently, the swirl angle, α, remains constant throughout the vaneless diffuser or the vaneless space in a vaned diffuser. This follows from the definition of the flow angle, $\tan(\alpha) = c_\theta / c_m$ and substitution of Eqs. 2.12 and 2.13, which gives Eq. 2.14.

$$\tan(\alpha_3) = \frac{c_{\theta 3}}{c_{m3}} = \frac{c_{\theta 4}}{c_{m4}} = \tan(\alpha_4) \tag{2.14}$$

2.2.2 Vaned Diffusers

Vaneless diffusers require a relatively large radius ratio to achieve sufficient diffusion since the reduction in the velocity components is only a function of the increase in radius [10]. While this is acceptable in industrial compressors, it becomes impractical in small compressors with strict geometric constraints. In such applications, vaned diffusers are used instead. The purpose of the vaned diffuser is to reduce the swirl imparted to the flow by the impeller. This increases the diffusion, which gives a larger pressure rise for the same radius ratio. The disadvantages of a vaned diffuser include; smaller stall and choke margins, higher friction losses due to higher wetted surface and more blockage as a result of larger boundary layers on the vane surfaces.

There are two main types of vaned diffusers, channel diffusers and curved vane diffusers [8], examples of which can be seen in Fig. 2.8. The first one, consists of vanes constructed to have a controllable channel width increasing area. This makes every individual channel resemble a 2D axisymmetric diffuser [11]. The diffusion is controlled by the area ratio (AR), the length to width ratio (L/W) and channel opening angle (2θ). Common AR and 2θ for wedged channel diffusers is between 1.4 and 2.0 and 10° to 14° respectively obtained from the Reneau charts [10].

2.2.3 Splitter Vanes

Inserting splitter vanes in to a diffuser increases the possibility of pressure recovery, but also blockage and friction. This allows for control of the half angle and therefore the diffusion downstream of the vane LE, allowing for a greater half angle at the first portion of the vanes [8].

In aero-engine applications, where the flow must be turned from radial to axial direction, vane trailing-edge geometries are particularly important. A rounded TE is generally preferred over wedge-shaped designs, since the wedge-shaped designs tend to generate large wakes. Within the radial-to-axial bend, the pressure gradient

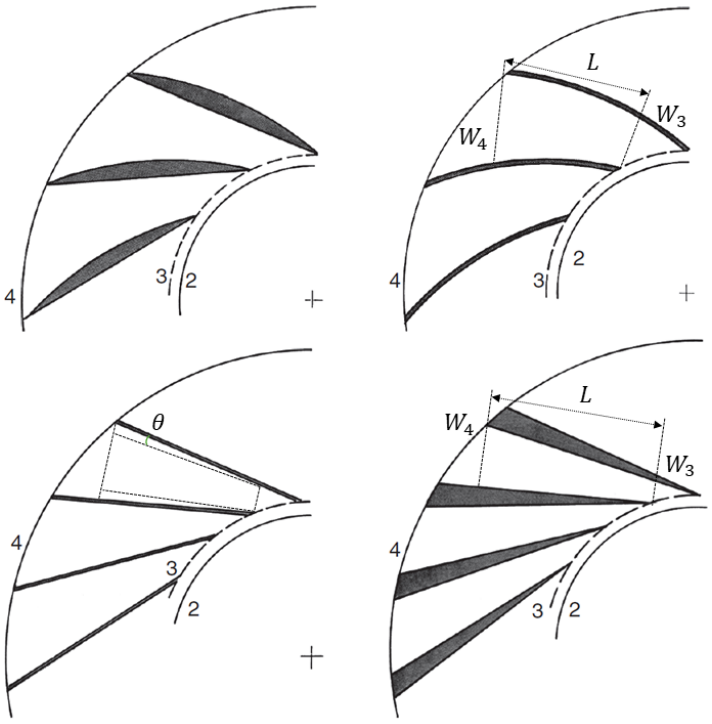

Figure 2.8: Curved vaned diffusers (top) and channel diffusers (bottom). Adapted from [8].

($\partial p/\partial r > 0$) points from the hub to the shroud, causing the wake structures from the TE of the vanes to migrate and collect near the hub. This creates a region of very low total-pressure being ingested by the downstream axial OGV. This requires additional axial distance for flow reattachment before the LE of the axial OGV, which is often limited in compact aero-engine configurations.

2.2.4 Impeller–Diffuser Interaction and Radial Gap

The region between the impeller TE and diffuser LE,$R_3 - R_2$ in Fig. 2.7, is referred to as the radial gap and can be considered as a short vaneless diffuser [2]. This region is susceptible to significant losses, as flow separation near the diffuser throat can lead to unsteady behaviour and oscillations [12]. Typical radius ratios for the radial gap (R_3/R_2) are in the range of 1.1-1.2 [6], although more compact designs, such as the NASA HECC [5], use values as low as 1.07.

2.2.5 Design Parameters

The throat area, positioned at W_3 in Fig. 2.8, is the smallest area normal to the flow between two adjacent vanes. It determines the choking massflow of the diffuser and in most cases subsequently the entire compressor. Throat matching of the diffuser and impeller throats is an important parameter for the operating range of

the compressor [10]. A relation of the throat areas is seen in Eq. 2.15. Where A_d^* and A_i^* is the diffuser and impeller throat areas. M_{u2} is the blade Mach number, defined as $M_{u2} = U_2/a_{01}$, λ is the work coefficient and γ is the ratio of specific heat. R_1 is the mean inlet radius of the impeller. For the case with splitter vanes, the throat between the main and splitter vanes can also become the limiting throat if placed to close to the main vanes throat.

$$\frac{A_d^*}{A_i^*} = \frac{\left[1 + ((\gamma-1)/2)(R_1/R_2)^2 M_{u2}^2\right]^{\frac{(\gamma+1)}{2(\gamma-1)}}}{\left[1 + (\gamma-1)\lambda M_{u2}^2\right]^{\frac{(\gamma+1)}{2(\gamma-1)}}} \tag{2.15}$$

The solidity (σ) of a vaned diffuser is defined as the ratio of chord length (l) to pitch (s), as given in Eq. 2.16, where $l = 2\pi R_3/Z$ and Z is the number of vanes. Diffusers may range from low-solidity designs ($\sigma < 1$) to high-solidity configurations ($\sigma > 2$). For highly loaded compressors with large pressure ratios and high inlet Mach numbers, higher solidity is generally preferred, as it reduces vane loading and improves flow guidance.

$$\sigma = \frac{l}{s} \tag{2.16}$$

2.3 Performance Parameters

In order to evaluate the aerodynamic quality of a diffuser, several performance parameters are commonly used. These coefficients quantify how effectively the diffuser converts kinetic energy into static pressure, as well as the losses associated with total pressure and kinetic energy recovery. The definitions used in this work follow standard turbomachinery conventions.

The pressure recovery coefficient, C_p, is the measure of the increase in static pressure across the diffuser normalised by the dynamic pressure at the inlet of the diffuser and is defined in Eq. 2.17. A large C_p means effective diffusion without an extensive amount of losses.

$$C_p = \frac{p_4 - p_2}{p_{02} - p_2} \tag{2.17}$$

The total pressure loss coefficient, ζ, quantifies the total pressure loss over the diffuser, normalised by the dynamic pressure at the inlet to the diffuser and is defined in Eq. 2.18.

$$\zeta = \frac{p_{02} - p_{04}}{p_{02} - p_2} \tag{2.18}$$

The kinetic energy recovery coefficient, ξ, represents the fraction of kinetic energy

remaining at the diffuser exit and is defined in Eq. 2.19.

$$\xi = \frac{p_{04} - p_4}{p_{02} - p_2} \tag{2.19}$$

The sum of C_p, ζ and ξ is by definition equal to unity.

Lieblein Diffusion Factor (DF) (Eq. 2.20) is a coefficient combining the mean deceleration (Term 1) and turning (Term 2) of the flow [2]. Although originally developed for axial compressor cascades, it is still commonly used as an indicative measure for other configurations. For axial machines, recommended values are around 0.45, with a maximum near 0.6 [2], these recommendations are however not fully applicable for a radial diffuser. The reason is that as stated in previous sections, in a radial diffuser, diffusion is dependent on the radius ratio, which is not the case for an axial diffuser.

$$DF = \underbrace{1 - \frac{c_2}{c_1}}_{Term\ 1} + \underbrace{\frac{c_{\theta 1} - c_{\theta 2}}{2c_1\sigma}}_{Term\ 2} \tag{2.20}$$

The de Haller number (DH) (Eq. 2.21) is a simpler parameter for determining diffusion. As seen it is part of Term 1 in the diffusion factor and only evaluates the deceleration of the flow. Again developed for axial machines, the recommended value is $DH \geq 0.72$.

$$DH = \frac{c_2}{c_1} \tag{2.21}$$

2.4 Computational Fluid Dynamics

Computational fluid dynamics is the numerical computations of fluid flow through the use of computers. The most standard practice is the use of the finite volume method which is a method to discretise the governing equations from partial differential equations to algebraic equations. A domain of which fluid sits or moves, is geometrically divided into many smaller elements, most often referred to as cells. The properties of the fluid, such as velocity, pressure and temperature is calculated and stored in the centre of the cells.

2.4.1 Governing Equations

The most fundamental principles governing fluid dynamics are the conservation of mass, the conservation of momentum, and the conservation of energy. Although these governing equations arise from different physical foundations, together they form the core mathematical framework used to describe fluid motion. Their full

derivations are extensive and well known to students and practitioners in the field, and therefore only a brief overview is provided here. For completeness, the equations are presented in their compressible, unsteady, differential, and tensor form.

The conservation of mass equation, or more commonly the continuity equation, suggest as the name states the mass of a fluid must be constant if there is no in- or outflow. The continuity equation is shown in Eq. 2.22.

$$\frac{\partial \rho}{\partial t} + \frac{\partial (\rho u_i)}{\partial x_i} = 0 \tag{2.22}$$

The conservation of momentum is derived from Newton's second law and describes how internal and external forces (right hand side) influence fluid motion (left hand side), as expressed in Eq. 2.23. This formulation actually consists of three separate equations, one for each spatial direction, collectively known as the Navier-Stokes equations.

$$\frac{\partial (\rho u_i)}{\partial t} + \frac{\partial (\rho u_i u_j)}{\partial x_j} = -\frac{\partial p}{\partial x_i} + \frac{\partial \tau_{ij}}{\partial x_j} + \rho f_i \tag{2.23}$$

The conservation of energy is the first law of thermodynamics applied to a fluid system. It states that the rate of change of internal energy within a fluid element must balance the work done on the fluid and the heat transferred to it, as expressed in Eq. 2.24. This equation form the foundation of the energy transport relation used in fluid dynamics and CFD simulations.

$$\frac{\partial (\rho e)}{\partial t} = -\frac{\partial (p u_i)}{\partial x_i} + \Phi + \frac{\partial}{\partial x_i}\left(\kappa \frac{\partial T}{\partial x_i}\right) \tag{2.24}$$

2.4.2 Turbulence Modelling

Turbulence modelling is the part of CFD that handles the elusive phenomena of turbulence. The seemingly chaotic, swirling behaviour of fluids is modelled through further manipulation of the momentum equation (Eq. 2.23) by applying Reynolds time averaging. This gives the Reynolds Average Navier Stokes (RANS) equations. These can be in steady-state or unsteady-state, the latter referred to as unsteady RANS. Time averaging gives rise to Reynolds Stresses which needs to modelled by extra equations and this is what turbulence modelling is about.

The $k - \varepsilon$ Model

The $k - \varepsilon$ is a two-equation turbulence model and one of the earliest developed. It models turbulent kinetic energy (k), see Eq. 2.25 and dissipation rate (ε), see Eq. 2.26. The model is good for free field flow, i.e. away from a the wall but needs

to be modelled in near wall flow if used.

$$\frac{\partial}{\partial t}(\rho k) + \frac{\partial}{\partial x_i}(\rho u_i k) = P_k + P_{kb} - \rho\varepsilon + \frac{\partial}{\partial x_i}\left[\left(\mu + \frac{\mu_t}{\sigma_k}\right)\frac{\partial k}{\partial x_i}\right] \tag{2.25}$$

$$\frac{\partial}{\partial t}(\rho\varepsilon) + \frac{\partial}{\partial x_i}(\rho u_i \varepsilon) = \frac{\varepsilon}{k}(c_{\varepsilon 1}P_k - c_{\varepsilon 2}\rho\varepsilon + c_{\varepsilon 1}P_{\varepsilon b}) + \frac{\partial}{\partial x_i}\left[(\mu + \sigma_\omega \mu_t)\frac{\partial \varepsilon}{\partial x_i}\right] \tag{2.26}$$

The $k-\omega$ Model

The Wilcox $k-\omega$ is a two-equation turbulence model [13]. It stems from the $k-\varepsilon$ model and models turbulent kinetic energy (k), see Eq. 2.27, and the specific dissipation rate (ω), see Eq. 2.28. The relation between ω and ε is $\varepsilon = \beta^*\omega k$, where $\beta^* = 0.09$. The model is good at modelling flow near the wall but has difficulties in presence of strong pressure gradients.

$$\frac{\partial}{\partial t}(\rho k) + \frac{\partial}{\partial x_i}(\rho u_i k) = P_k + P_{kb} - \beta^*\rho k\omega + \frac{\partial}{\partial x_i}\left[\left(\mu + \sigma^*\frac{\rho k}{\omega}\right)\frac{\partial k}{\partial x_i}\right] \tag{2.27}$$

$$\frac{\partial}{\partial t}(\rho\omega) + \frac{\partial}{\partial x_i}(\rho u_i \omega) = \alpha\frac{\omega}{k}P_k + P_{\varepsilon b} - \beta\rho\omega^2 + \frac{\partial}{\partial x_i}\left[(\mu + \sigma_\omega\mu_t)\frac{\partial \omega}{\partial x_i}\right] \tag{2.28}$$

The Shear Stress Transport Model

The Menter Shear Stress Transport (SST) model [14] is a two-equation model which models the turbulent kinetic energy, k, and dissipation rate, ω. It blends the $k-\omega$ model in the near wall flow and the $k-\varepsilon$ in the freestream flow. The transport equations for k and ω are presented in equation Eq. 2.29 and 2.30 respectively.

$$\frac{\partial}{\partial t}(\rho k) + \frac{\partial}{\partial x_i}(\rho u_i k) = \tilde{P}_k - \beta^*\rho k\omega + \frac{\partial}{\partial x_i}\left[(\mu + \sigma_k\mu_t)\frac{\partial k}{\partial x_i}\right] \tag{2.29}$$

$$\frac{\partial}{\partial t}(\rho\omega) + \frac{\partial}{\partial x_i}(\rho u_i \omega) = \alpha\rho S^2 - \beta\rho\omega^2 + \frac{\partial}{\partial x_i}\left[(\mu + \sigma_\omega\mu_t)\frac{\partial \omega}{\partial x_i}\right] + 2(1-F_1)\rho\sigma_{w2}\frac{1}{\omega}\frac{\partial k}{\partial x_i}\frac{\partial \omega}{\partial x_i} \tag{2.30}$$

Here, F_1 is the important blending function which determines if the $k-\omega$ or the $k-\varepsilon$ is the dominant model depending on how close to a wall the flow is. The SST model is substantially more accurate for flows with strong adverse pressure gradients and pressure induced separation, hallmark for aeronautical and turbomachinery simulations.

2.4.3 Wall Treatment

With turbulence modelling comes also the subject of wall treatment. The flow close to walls can either be resolved by having a fine enough boundary layer meshed, or be modelled by wall functions. Fine enough means that the y^+ value of the first wall cell is less than unity, where y^+ is the dimensionless wall distance. This is the recommended practice for SST and $k-\omega$. The definition for y^+ is seen in Eq. 2.31;

$$y^+ = \frac{u^* y}{\nu} \tag{2.31}$$

where u^* is the friction velocity, y is the first cell height and ν the kinematic viscosity. If the boundary layer is not resolved and instead modelled the value of y^+ needs to be $y^+ < 5$ or $30 < y^+ < 500$. Between 5 and 30 is called the buffer layer and there exist no model for this region. For $y^+ < 5$, the boundary layer is modelled with Eq 2.32;

$$u^+ = y^+ \tag{2.32}$$

where u^+ is the dimensionless orthogonal velocity close to the wall. If $30 < y^+ < 500$ the boundary layer is modelled by Eq. 2.33;

$$u^+ = \frac{1}{\kappa} \ln y^+ + B \tag{2.33}$$

Where $\kappa \approx 0.4$ is Von Kárman's constant and $B \approx 5.5$ is an empirical constant. This is the common practice when using the $k-\varepsilon$ model.

3

Methodology

This chapter presents the methodology used in this thesis work. First an overview of the approach is presented, followed by the validation study of NASA HECC impeller and the CFD setup. Lastly, the design constraints and targets for the diffuser study and the different diffuser designs tested are presented.

3.1 Approach and analysis

An extensive literature review on basic centrifugal compressor theory is done and presented in the previous chapter. The publicly available impeller geometry from NASA HECC is used as the impeller geometry in this thesis work. The geometry of the NASA HECC impeller is recreated using publicly available information in ANSYS BladeGen 2024R2®. The generated geometry is meshed in ANSYS Turbogrid 2024R1®. Three-dimensional, steady-state simulations are performed, using a single blade passage for the impeller only simulations, in ANSYS CFX 2024R1®. The thesis work is divided into two distinct parts. The first part of the thesis presents a numerical validation study of NASA HECC impeller. The second part of this thesis work evaluates different diffuser designs.

The numerical validation study of the centrifugal impeller includes a mesh independence study and a steady-state turbulence model study. The turbulence model study compares the Wilcox $k-\omega$, $k-\varepsilon$, and the SST model to determine the most appropriate turbulence model. The numerical results from this validation study is compared to numerical and experimental data from NASA.

The numerically validated impeller is then used to test a variety of diffuser concepts. Namely, wedge shaped and cascade airfoils are compared in terms of their diffusion capabilities and their impact on the operating range of the compressor. Additionally, the use of splitter vanes in radial diffusers is extensively investigated. The different diffusers are evaluated using the performance parameters mentioned in Sec. 2.3.

3.2 Geometry

The geometry of the HECC is open source and the impeller is therefore chosen as a reference for the diffuser simulations done in this thesis. This section describes the HECC impeller geometry, operating conditions, pressure ratio and other performance parameters for which the validation study have been done.

3.2.1 Impeller Geometry

Two sets of geometric data have been made available by NASA for the HECC impeller, i.e., the design intent and the manufactured design as presented in Tab. 3.1 from [15]. The numerical studies performed by NASA is for the design intent geometry, while the experimental data made available by NASA is for the manufactured geometry. The data presented for the design intent geometry in Tab. 3.1 is for the "hot geometry". The data presented in Tab. 3.1 for the manufactured geometry is for the "cold geometry".

Hot geometry is the geometry of the impeller when it is rotating at its design speed, while the cold geometry is when the impeller is stationary. Spinning up the cold geometry should yield the hot geometry, i.e., cold geometry + rotational mechanical loads + thermal stresses should yield the hot geometry. As can be observed from the data in Tab. 3.1, the cold geometry has smaller radii at the hub and the shroud of the impeller blades to accommodate for the rotational and thermal expansions.

Here it is noted that, NASA notes differences between the design intent (hot) and the manufactured (cold) geometry which cannot be attributed to the hot-to-cold conversion [15]. The main differences are noted at the splitter LE metal angle, impeller exit radius and blade thickness for both blades [15]. These differences noted by NASA also contribute to the uncertainties in the numerical work presented in this thesis. The geometric uncertainties in splitter LE metal angle and the thickness distribution directly influence the throat at any given blade span, and as illustrated Eq. 2.15 the throat directly determines choking massflow of the impeller. Additionally, the definitions of backsweep, lean and rake are provided in Sec. 3.2.2.

The curve coordinates for the meridional flow path given in [5] are plotted in Microsoft Excel and the positioning of splitter LE, R_{h1}, R_{s1}, R_2, b_2 and s_{tip} from Tab. 3.1 is used. The meridional flow path is illustrated in Fig. 3.1. In Ansys BladeGen, curves are defined with Bezier points. These are adjusted manually, and the curves are exported, plotted and compared with the outline curves provided in [5]. This is done iteratively until a close match is achieved. However, the upstream bend illustrated in Fig. 3.1 from axial position 0 mm to –134 mm has not been incorporated in computational domain and has instead been considered as a straight channel from 0 mm to –60 mm, axial position.

Table 3.1: Impeller Geometry Data, obtained from [15].

Parameter	Design intent (hot) [mm]	Manufactured (cold) [mm]
R_{h1}	40.513	40.437
R_{s1}	107.696	107.645
Splitter R_{h1}	67.513	66.802
Splitter R_{s1}	120.320	120.320
R_2 Hub	215.748	215.392
R_2 Shroud	215.875	215.443
R_2 Average	215.824	215.417
b_2	15.469	15.24
s_{tip}	0.3048	0.3048
Z, Main/Splitter	15/15	15/15
Backsweep	30°	30°
LE Lean	-2°	-2°
TE Rake	-29°	-29°

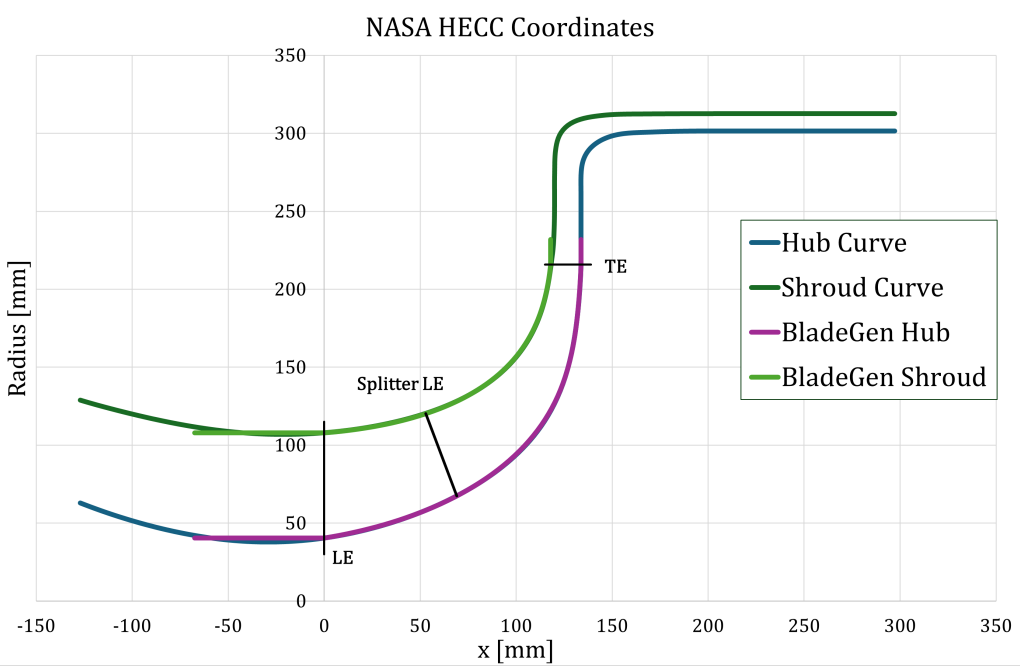

Figure 3.1: Meridional view of the NASA HECC flow path with impeller LE, splitter LE, and impeller TE marked hub, shroud and splitter blades for HECC impeller, plotted with coordinates obtained from [5].

3.2.2 Impeller Blades and Splitter Geometry

The impeller blade is defined geometrically by radially stacking five different blade profiles at five blade spans (0, 25, 50, 75 and 100%) along their respective centroid, as is illustrated in Fig. 3.2. Each blade profile at a specified blade span is defined using the blade angle distribution and the thickness distribution.

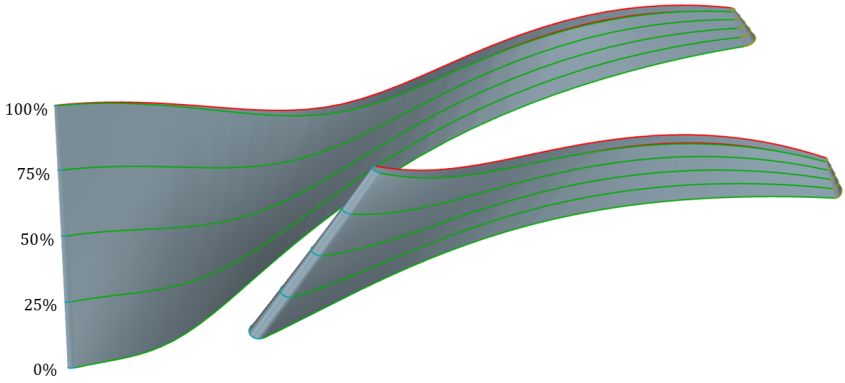

Figure 3.2: Radial stacking of the five blade spans.

In Ansys BladeGen, the blade angle (β) distribution and theta (θ) define the blade geometry along the meridional flow path (ΔM). The blade angle distribution describes how the local blade metal angle changes from the LE to the TE along a streamwise location (Eq. 3.1). This distribution directly controls the flow turning, diffusion, and aerodynamic loading of the blade, making it essential for achieving desired performance characteristics such as pressure rise and efficiency. A smooth and carefully tailored blade angle distribution helps avoid flow separation and excessive losses, especially in high-loading regions.

$$\beta = \arctan\left(\frac{\Delta\theta \cdot rad}{\Delta M}\right) \tag{3.1}$$

The theta distribution, on the other hand, represents the circumferential position of the blade as a function of the meridional distance (Eq. 3.2). In BladeGen, θ is used to construct the actual three dimensional blade shape by integrating the blade angle along the flow path. Essentially, while the blade angle defines the local flow direction relative to the blade, the theta distribution determines how the blade wraps around the axis of rotation.

$$\Delta\theta = \tan(\beta) \cdot \Delta M \tag{3.2}$$

The blade angle distribution and $\theta-$distribution also defines backsweep, lean and rake. Backsweep is the blade metal angle at the impeller TE (β_2 in Fig. 2.4). The backsweep angle determines the absolute velocity at the exit of the impeller (c_2 in Fig. 2.4). The absolute velocity at the impeller exit is inversely proportional to the

backsweep angle, i.e., a higher backsweep angle leads to lower absolute impeller exit velocity and correspondingly lower total pressure rise achieved. However, a higher backsweep angle also allows for a greater operating range. Lean is the difference in θ from the hub to the shroud at the LE and rake is the difference compared to the rotational axis.

The blade angle distribution for the NASA HECC impeller is not explicitly provided in tabulated form and is therefore obtained by digitising available graphical data from [5]. The splitter blade follows the same angular distribution as the main blade and is placed circumferentially midway between two main blades. The blade angle distributions for the main and splitter blades are presented in Fig. 3.3. The splitter blade LE is positioned at 30.8% of impeller meridional length. The blade metal angle for both the main and splitter blades follow the typical "S"-shape, seen in most centrifugal impellers, i.e., a decreasing blade metal angle from the LE to approximately the mid chord length and increasing thereafter to the TE to introduce a backsweep angle.

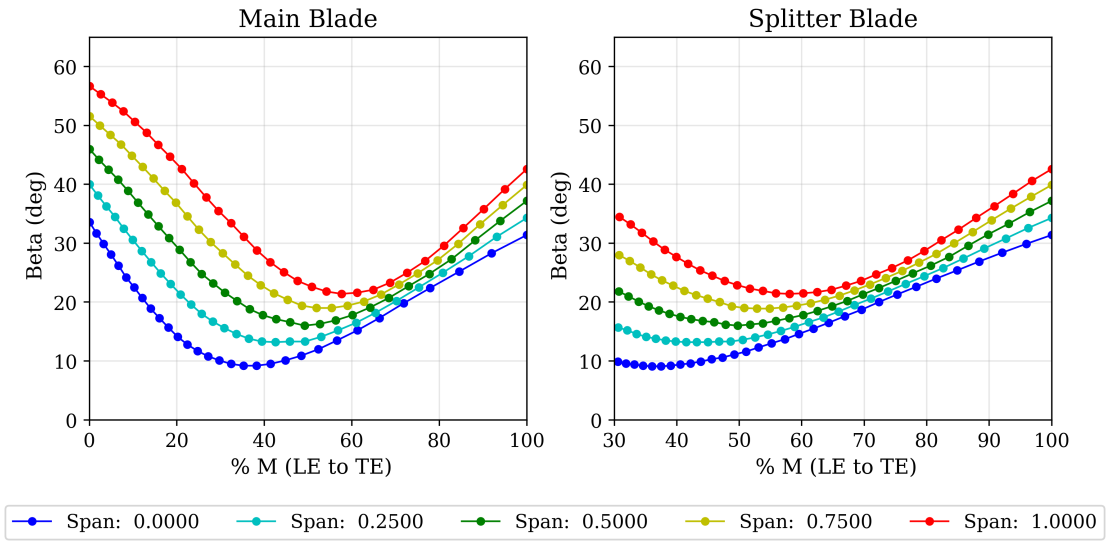

Figure 3.3: HECC impeller blade angles, main blades (left) and splitter blades (right).

For this particular impeller blade, the blade metal angle at the LE of the main blade is seen to change from 32° at the hub to 58° at the tip. Similarly for the splitter blade the blade metal angle is 10° at the hub and 35° at the tip. In the same way the TE angle for the main and the splitter blade changes from 31° at the hub to 42° at the tip.

The blade thickness distribution is derived in a similar manner. In Fig. 3.4, a difference between the NASA derived and generated thickness profiles for the main blade can be seen. The original data suggests a piece-wise linear distribution, which results in non-smooth blade geometry. Therefore, a smoother thickness distribution is assumed. The splitter thickness is adjusted independently to avoid an excessively thick LE. The impeller throat area is obtained from Ansys BladeGen to be 20011 mm^2. The replicated geometry is seen in Fig. 3.5.

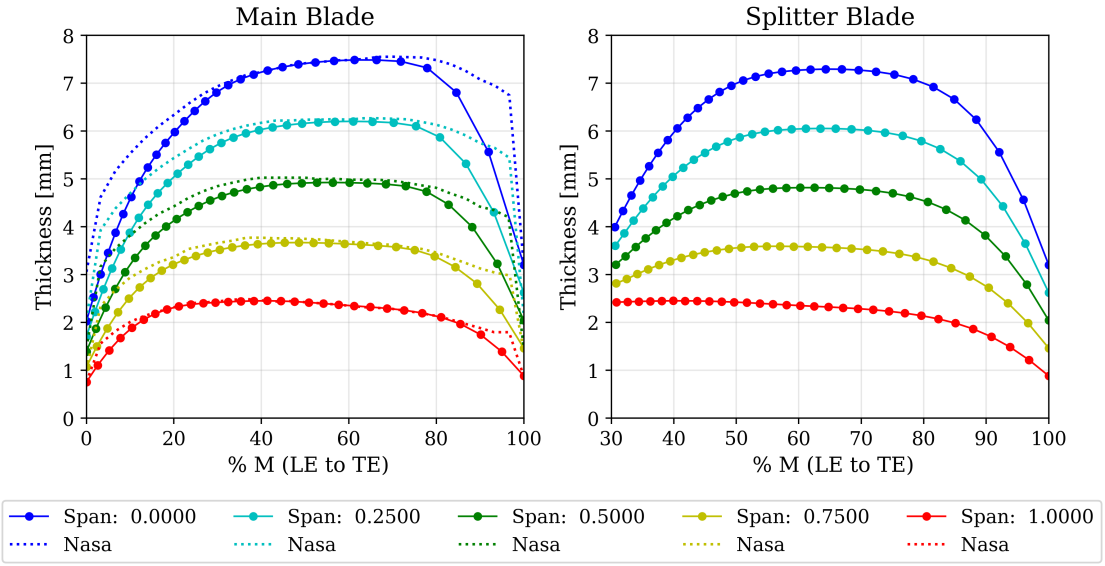

Figure 3.4: HECC impeller blades normal thickness, main blades (left) and splitter blades (right).

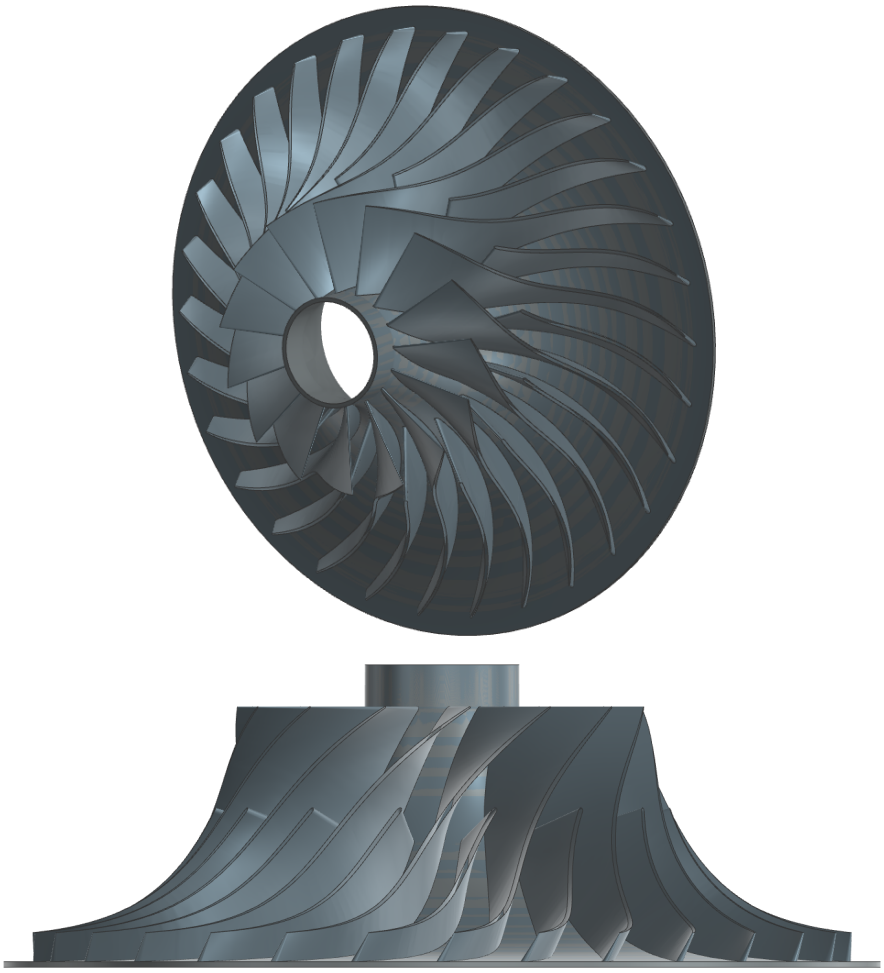

Figure 3.5: Isometric (top) and side/top (bottom) view of the replicated HECC impeller.

3.2.3 HECC Vaned Diffuser

The HECC diffuser is a vaned diffuser with splitter vanes, in total 20 of each. The outline geometry data is presented in Tab. 3.2. No additional accurate data, such as vane angle and thickness distribution is presented. The decision to not validate the diffuser also is made because of the much larger number of uncertainties this implies. Instead, the overall dimensions of the vaned diffuser (R_3, R_4, b_3) are used as constraining parameters for the designed diffusers.

Table 3.2: Geometry of the NASA HECC Vaned Diffuser, obtained from [5, 15].

Parameter	Value
R_3	231.343 mm
R_4	284.455 mm
b_3	14.199 mm
Z, Main/Splitter	20/20

3.3 Validation Study of NASA HECC Impeller

Steady-state RANS (Sec. 2.4.2) simulations are performed at the ADP. The design rotational speed is 21897 RPM in a counter-clock wise direction [5]. The inlet conditions is standard sea level static atmospheric, i.e., total temperature of 288.15 K and total pressure of 1 atm. The design massflow recommendation varies depending on which diffuser configuration is implemented [15], for analysis 4.99 kg/s is recommended. The total pressure ratio for this operating point is not explicitly stated. From linear interpolation the total pressure ratio is approximately 5.23 for the impeller only. The operating conditions is summarised in Tab. 3.3.

Table 3.3: Performance of the NASA HECC Impeller Only, obtained from [5, 15].

Parameter	Value
$\dot{m}$	4.99 kg/s
Ω	21897 RPM
U_2	492.45 m/s
p_{01}	1 atm
T_{01}	288.15 K
PRTT	5.23
λ	0.79

3.3.1 CFD Setup and Domain

Three-dimensional, steady-state simulations are done on a single blade-passage with rotational periodic boundary conditions to represent the full annulus. The computational domain consists of an inlet duct, a rotating impeller, and a stationary outlet domain, as shown in Fig. 3.6. For impeller-only simulations, the outlet domain represents a vaneless configuration. For diffuser simulations, the outlet domain includes the diffuser geometry. A stage mixing-plane interface is used between rotating and stationary domains. The inlet to the computational domain is prescribed as total pressure inlet. The total pressure inlet is defined with a total temperature of 288.15°K, a turbulence intensity of 5%, a total pressure of 1 atm and velocity components as normal to the boundary. The outlet to the computational domain is prescribed as a static pressure outlet as the average over the whole outlet area. The outlet pressure is changed to match the required massflow. To obtain a speedline, the static pressure at the exit of the computational domain is changed in steps of 20 kPa near choke to finer refinements of 2.5 kPa close to stall. The finer refinements close to stall conditions are necessary to identify the stall point accurately. The larger steps of 20 kPa near choke is acceptable as no changes are expected in the flow in choke conditions.

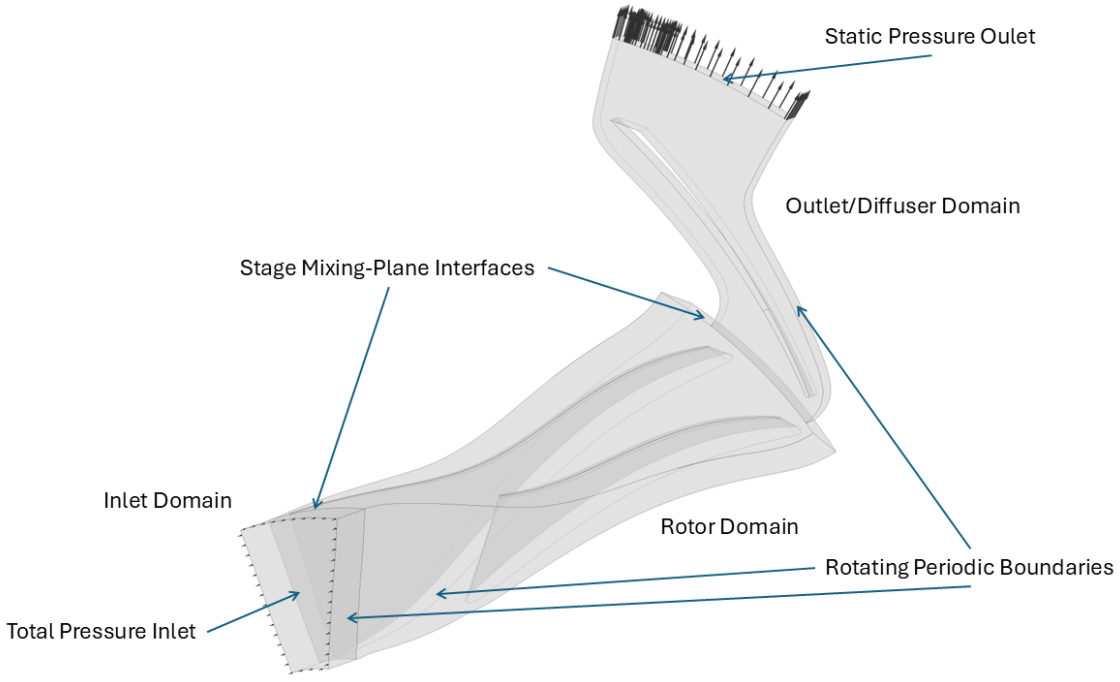

Figure 3.6: View of the CFD domains, here with a vaned diffuser.

3.3.2 Mesh Independence Study

A mesh independence study is conducted for the impeller using steady RANS simulations with the SST turbulence model at the ADP conditions. Three meshes are generated, the finer mesh is at least 2.19 times finer than the coarser mesh [16].

Boundary layer resolution is ensured with $y^+ < 1$. The mesh sensitivity of the results is evaluated based on the total pressure ratio and isentropic efficiency. Figure 3.7 illustrate the low-Re medium grid, in a blade-to-blade view, used in the mesh independence study.

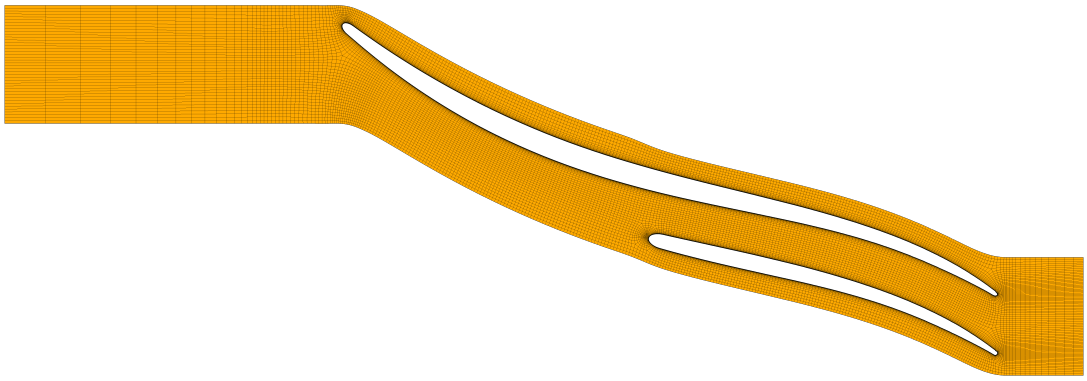

Figure 3.7: Low-Re medium grid in a blade-to-blade view.

To evaluate if mesh independence is achieved, Richardson extrapolation together with the Grid Convergence Index (GCI) is used. The idea behind the method is that the numerical error decreases as the mesh is refined, following a predictable trend. By comparing results from different grid sizes, it is possible to estimate how the solution would behave for an infinitely fine mesh. The observed convergence is then used to calculate the GCI, which provides an estimate of the numerical uncertainty in percentage form and helps determine whether the solution is independent of the grid [16].

3.3.3 Turbulence Models Comparison

A comparison of three different turbulence models is done with the main mesh settings from the result of the mesh independence study. The three turbulence models tested are $k-\varepsilon$, standard $k-\omega$ and SST. The same mesh is used $k-\omega$ and SST. For $k-\varepsilon$, the boundary layer is adjusted such that $y^+ > 30$ is achieved.

3.4 Diffuser Study

The aim with the diffuser study is to design a diffuser with either the same radius ratio R_4/R_2 as the NASA HECC diffuser and achieve a better performance, i.e., higher C_P and lower ζ, OR a smaller radius ratio R_4/R_2 than the NASA HECC diffuser and achieve equal or similar performance. The starting point for the diffuser study is a vaneless diffuser with $R_4/R_2 = 1.318$, identical to NASA HECC.

A Vaneless Diffuser (VLD) is created in Ansys BladeGen with the geometric outline as in Tab. 3.2. The results from this vaneless diffuser serves as the minimum

performance requirements for the vaned diffuser case. The impeller exit flow profiles from the vaneless case also serves as input to the vaned diffuser case (α_2 and M_2). The geometric parameters (R_4, R_3, b_3) from the vaneless diffuser geometry is also used to define the vaned diffuser geometry. Two different types of vanes are evaluated for the vaned diffuser geometry; wedge vanes and cascade vanes (Fig. 2.8).

As mentioned in Sec. 2.2.5 the throat area is an important criteria to consider during diffuser design to ensure matching of the choking massflow between the impeller and the diffuser. Failure to accurately match the throat area can lead to severe loss of operational range. Here it is noted that the geometrical throat is not necessarily the aerodynamic throat. Typically, the aerodynamic throat is smaller than the geometric throat due to the formation of boundary layers on the blade surfaces, flow separation, shock formation on suction side of the vane. Therefore it is also important to ensure that the blade metal angles at the diffuser LE is well matched to the incoming flow to prevent any large incidence angles which promote flow separation.

Several studies have illustrated that defining the blade metal angle at the diffuser LE as the average swirl angle exiting the impeller (α_2) is sufficient to achieve low incidence angles at the diffuser LE [10]. Therefore, the blade metal angle at the LE of the diffuser of all investigated cases is set at a constant value from the hub to the tip and is set equal to the average flow angle exiting the impeller at the ADP. The throat area of the diffuser and its position along the chord can be controlled with the blade angle distribution and the thickness distribution of the vanes. The required impeller to diffuser throat area ratio is calculated with Eq. 2.15 to $A_d^*/A_i^* = 0.252$, with $M_{u2} = 1.447$.

The wedged vanes are designed to have a linear increasing thickness and linear decreasing blade angle from the vane LE to the vane TE. The thickness changes from 1.5 mm at the LE and 6 mm at the TE. The LE is elliptical with an elliptic ratio of 2. The TE is cut-off, i.e., the same radius along the entire TE. The LE blade angle is set to the mean swirl angle analysed from the results of the vaneless case at the gap ratio $R_3/R_2 = 1.072$. This vaneless gap ratio is maintained for all investigated diffuser designs. The blade metal angle changes by 14.5° from the LE to the TE. Figure 3.8a shows a 2D view of the wedge vanes, this case is referred to as Wedged Diffuser (WD).

To address wake-related losses associated with wedge-shaped vanes, a Cascade Diffuser (CD) with circular-arc vane profiles is designed. The thickness distribution follows conventional airfoil design guidelines, with a maximum thickness of 3.5% at 30% chord. Figure 3.8b illustrate this design in 2D. Splitter vanes are added to both wedge and cascade configurations. The LE of the splitter vanes are place downstream of the main vane LE and downstream of main vane throat position. The LE definition of the splitters are the same as for the main vane. The splitters are placed circumferentially midway between two adjacent main vanes. These configurations are referred to as Wedged Splitter Diffuser (WSD) and Cascade Splitter Diffuser (CSD) and are illustrated in 2D in Fig. 3.8c and 3.8d respectively.

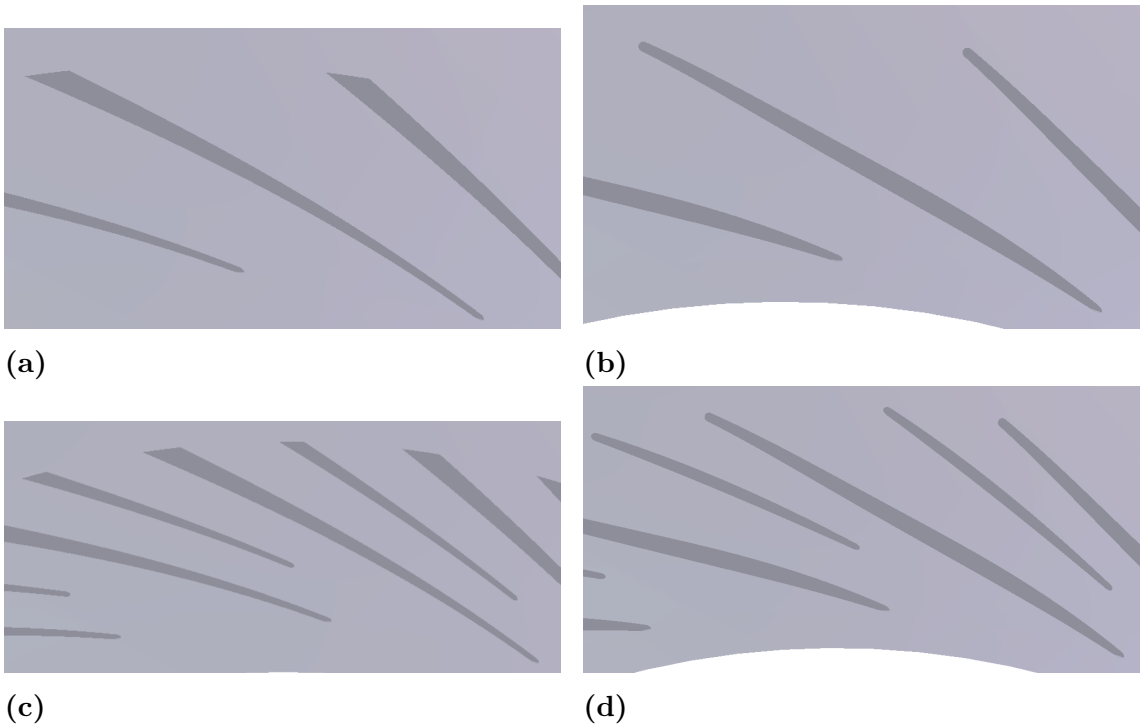

Figure 3.8: BladeGen Model and 2D view of the a) Wedged Diffuser, b) Cascade Diffuser, c) Wedge Splitter Diffuser and d) Cascade Splitter Diffuser.

All four diffuser designs have a vane metal angle at the LE of 72.5° and 58° at the TE. All four diffusers consists of 23 main vanes and the splitter designs (WSD and CSD) also consist of 23 splitter vanes. The geometric throat area of the wedged diffusers are 6807.83 mm^2 and for the cascade diffusers the throat area is 6306.60 mm^2. Noted for this is that the throat area ratios is between 0.34 and 0.32 respectively, which is larger than the calculated ratio of 0.252 according to Eq. 2.15. The reasoning for this is to leave space for the decrease to the aerodynamic area.

Figure 3.9 shows the increase in area within the vaned region. The blue curves for WD and WSD clearly illustrate the linear area increase of the straight channel. The sudden change at approximately 30% of the meridional length corresponds to the splitter LE, after which the rate of area increase becomes less steep. A similar effect is observed in the red curves for CD and CSD. However, instead of a distinct drop, the graph only changes gradient, with a more continuous and less steep increase in area. The area ratios, length-over-width ratios and solidity this corresponds to are presented in Tab. 3.4.

Table 3.4: Area ratio, length over width and solidity of the diffusers.

Ratio	WD	WSD	CD	CSD
AR	1.91	1.69	2.25	2.11
L/W	2.55	2.55	2.75	2.11
σ	1.66	1.66	1.64	1.64

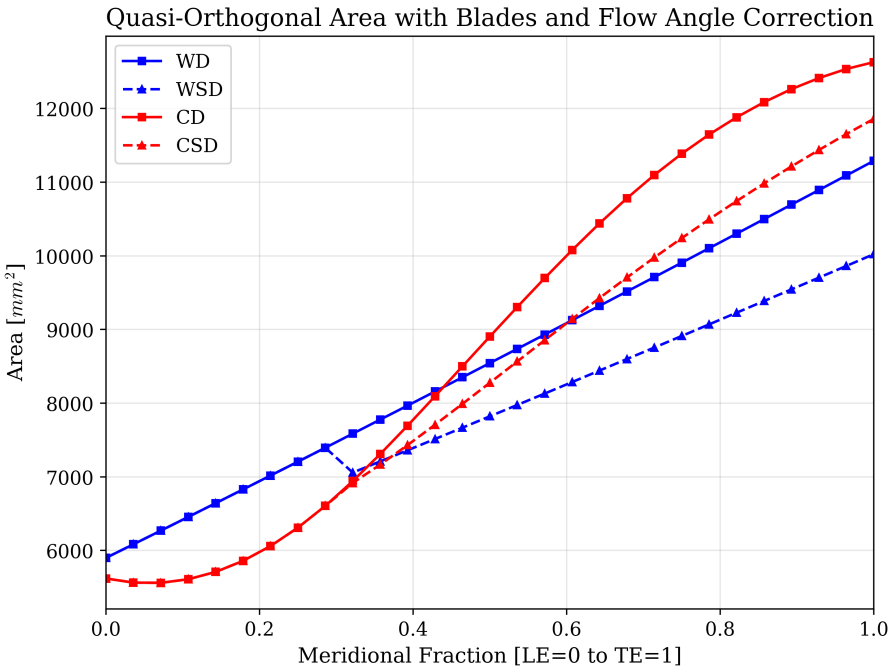

Figure 3.9: Quasi-Orthogonal Area increase of the different diffusers.

4

Results and Discussion

This chapter presents the results from validation study of the NASA HECC impeller and the diffuser design study.

4.1 Impeller Validation

The aerodynamic performance of the NASA HECC impeller is evaluated using the total pressure ratio (PRTT) and the isentropic efficiency (η_{is}) and is compared against NASA's numerical and experimental data at ADP and for the 100% speed-line. Experimental data from NASA [5] is presented as averaged data at probe locations in the experimental rig. The numerical data presented in this thesis work is compared against NASA's pre-experimental CFD simulations which were performed with the design intent geometry presented in Tab. 3.1.

As discussed previously in Sec. 2.2.1 the vaneless space downstream the impeller TE acts as vaneless diffuser and contributes to total pressure losses. Therefore, the radial extent of the computational domain downstream of the impeller TE is an uncertainty for the numerical validation study performed in this thesis work. For the numerical results presented by NASA, a single blade passage has been modelled into the computational domain and the Wilcox $k-\omega$ has been used as the turbulence model [5].

4.1.1 Mesh Independence Study HECC Impeller

The result from the mesh independence study for the design point presented in Tab. 3.3 is presented in Tab. 4.1. All meshes have a y^+ less than unity, i.e., low-Re grid which resolves the boundary layer as recommended for the SST turbulence model (Sec. 2.4.2). The number of cells are increased by approximately 2.19 times from coarse to medium and medium to fine grids. The cell count has been increased in a homogeneous manner to achieve finer grids.

From Tab. 4.1 it is observed that a monotonic convergence is achieved for both PRTT and η_{is}. A 0.113% difference in PRTT is observed between the coarse and medium grid. A 0.0 % difference in PRTT is observed between the medium and

fine grid. A 0.333% difference in η_{is} is observed between the coarse and medium grid. A 0.077% difference in η_{is} is observed between the medium and fine grid. The convergence trends for PRTT and η_{is} is illustrated in Fig. 4.1.

The Grid Convergence Index (GCI) for the fine grid is calculated to be approximately 0.46% for η_{is}. Since the difference in PRTT is zero, the Richardson extrapolation breaks down. The relative difference between the medium and fine grid solutions is only 0.00077%, which is several orders of magnitude smaller than the estimated numerical uncertainty. This indicates that the solution has reached grid independence, and the medium grid provides sufficient accuracy for the present analysis. The medium grid is chosen for all future simulations presented in this work owing to the less computational resources required compared to the fine grid.

Table 4.1: Mesh Study Results for HECC Impeller.

Grid	Domain	Cells	PRTT [−]	η_{is} [%]	y^+
Coarse	IC R1 S1	19292 849069 29150	5.301	93.789	0.887
Medium	IC R1 S1	39360 1864890 46800	5.295	94.030	0.891
Fine	IC R1 S1	77958 4056250 130640	5.295	94.102	0.777

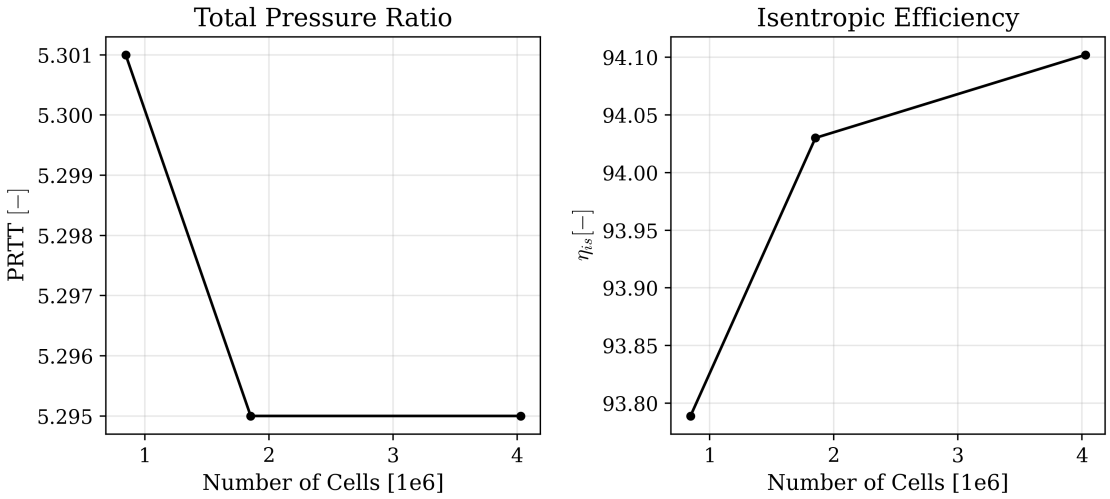

Figure 4.1: Results of the mesh independence study visualised.

4.1.2 Turbulence Models Comparison

The results from the turbulence model comparison is presented in Tab. 4.2. The y^+ for the $k-\omega$ and SST mesh achieved is 0.8 using a first cell distance of 1.0 μm. For the $k-\varepsilon$ the y^+ achieved is 52 using a first cell distance of 100 μm, i.e., wall functions are used to model the boundary layer.

All models overpredict PRTT and η_{is} compared to NASA's numerical data. In Tab. 4.3 the difference in percent between the three turbulence model tested and NASA's numerical data is presented. The standard $k-\omega$ is the closest match to NASA's numerical data with a difference of 1.109% for PRTT and 3.935% for the isentropic efficiency. In comparison for the SST turbulence model, an overprediction of 1.243% and 3.943% is observed for PRTT and η_{is} respectively. The largest difference is observed for the $k-\varepsilon$ turbulence model, with an overprediction of 1.587% for PRTT and 3.999% for η_{is} compared to NASA's numerical data.

Minimal differences are seen between the $k-\omega$ turbulence model and the SST turbulence model. The SST turbulence model has the benefit of improved prediction of adverse pressure gradients and mixing flow fields (Sec. 2.4.2). This is beneficial for the diffuser study. Therefore, the SST turbulence model with the low-Re, medium grid is selected for further simulations.

Table 4.2: Results from simulations with different turbulence models.

Model	PRTT [−]	η_{is} [%]
NASA	5.23	90.463
$k-\varepsilon$	5.313	94.081
$k-\omega$	5.288	94.023
SST	5.295	94.030

Table 4.3: Difference in percent between results from the turbulence model comparison.

Model	PRTT Δ(%)	η_{is} Δ(%)
NASA	-	-
$k-\varepsilon$	1.587	3.999
$k-\omega$	**1.109**	**3.935**
SST	1.243	3.943

4.1.3 Flow Field at ADP

Figure 4.2 illustrates the relative Mach number a constant 50% blade span. In Fig. 4.2 the position of the stagnation point of the LE indicates a slight positive

angle of incidence. The flow is seen to accelerate around the LE, leading to the formation of the suction peak. At 50% blade span the flow is still subsonic. However the strong suction peak is observed to produce a small suction side flow separation. The flow diffuses from the LE of the main blades to the splitter LE, as seen from the decreasing relative Mach number contour. A small positive angle of incidence is also observed at the splitter LE. The collection of the low momentum fluid from the tip region is observed at the TE of both the main and splitter blades. Similar flow features are observed at 25% and 75% blade spans in Fig. 4.3 and 4.4 respectively. However, it is seen that with the increasing blade span the relative inlet Mach number increases. Additionally the low momentum fluid from the tip clearance occupies a larger portion of the blade passage with increasing blade span.

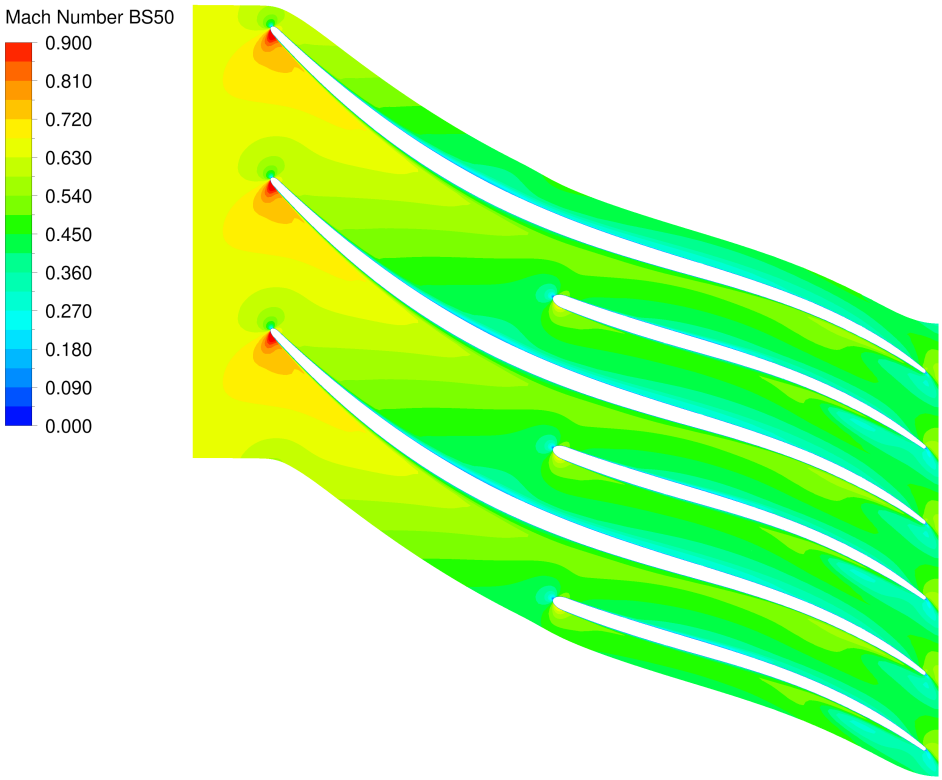

Figure 4.2: Impeller relative Mach number at 50% blade span.

The blade pressure distribution for the main blade and splitter blade at 50% blade span is illustrated in Fig. 4.5. The flow acceleration around the LE on both the pressure and the suction side of the main and the splitter blades can be visualised by the sudden drop in pressure (acceleration of the flow) at normalised stream-wise position 0.0 and 0.3 respectively. Normalised stream-wise position 0.0 and 0.3 mark the LE of the main and the splitter blades respectively. The sharp increase in pressure with increasing normalised stream-wise position represents the centrifugal effect. A small decrease in pressure is observed on the pressure side of the main blade at the splitter LE as a result of the suction peak (low pressure zone) on the splitter blade interacting with the pressure side of the main blade. The crossover of the pressure and suction side lines at the TE of the main and splitter blades is a

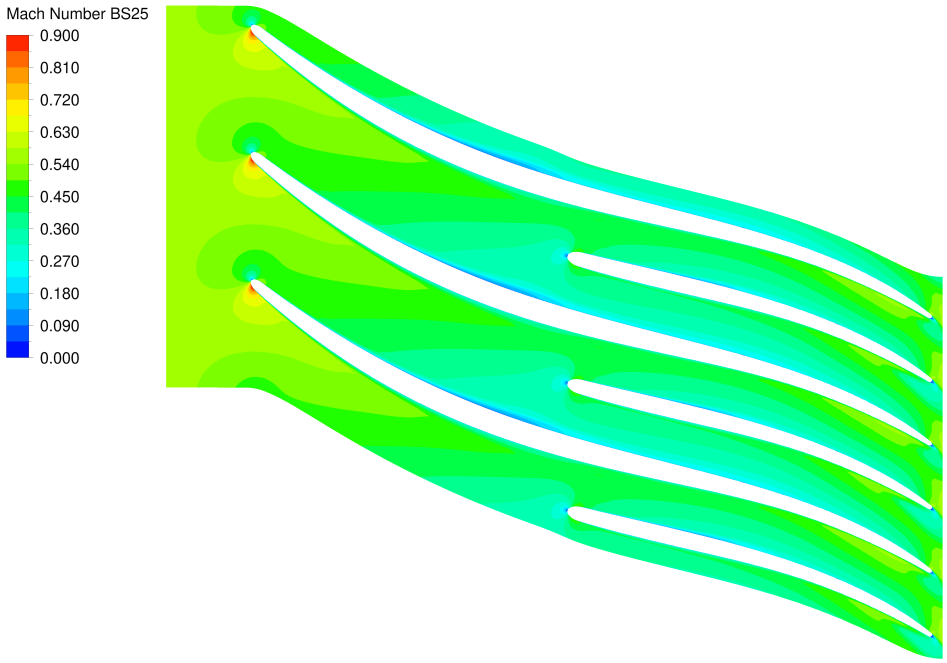

Figure 4.3: Impeller relative Mach number at 25% blade span.

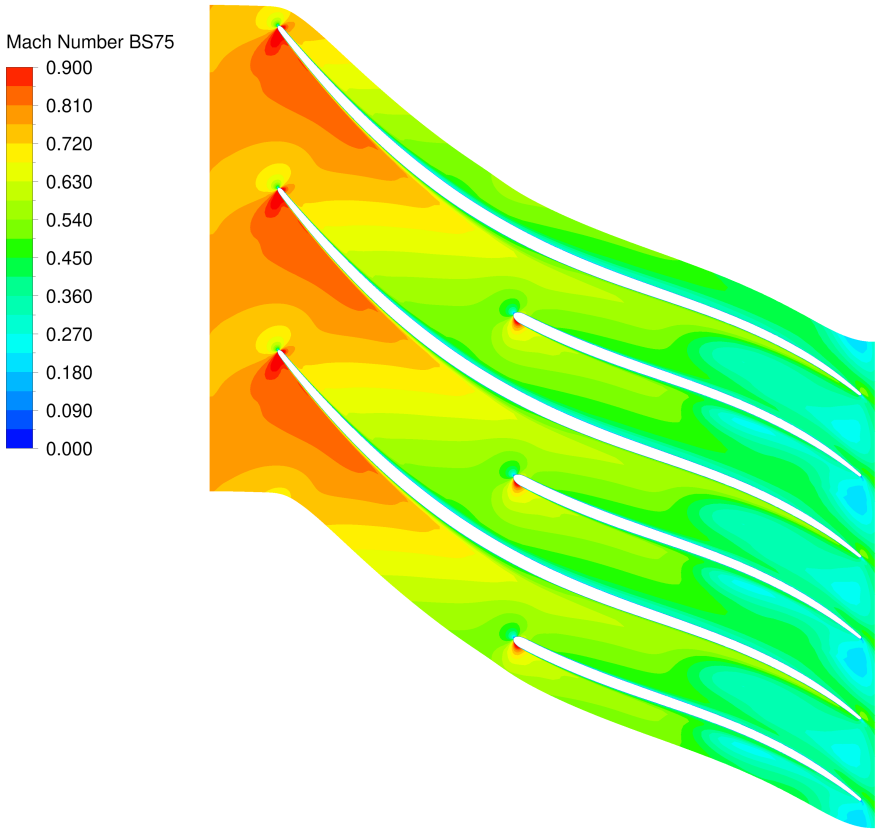

Figure 4.4: Impeller relative Mach number (bottom) at 75% blade span.

numerical artifact.

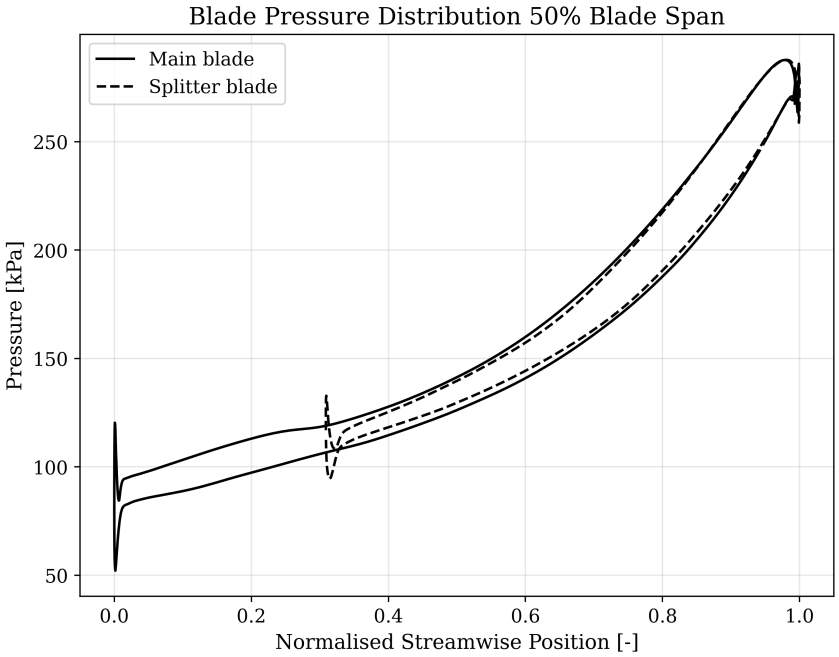

Figure 4.5: Pressure distribution along the impeller blades at 50% blade span.

Starting from the contour in Fig. 4.2, and more clearly visible in Fig. 4.4, low-momentum zones are observed at the TE. The tip-clearance flow is illustrated by the streamlines in Fig. 4.6, which extend downstream of the rotor and feed into these low-momentum regions.

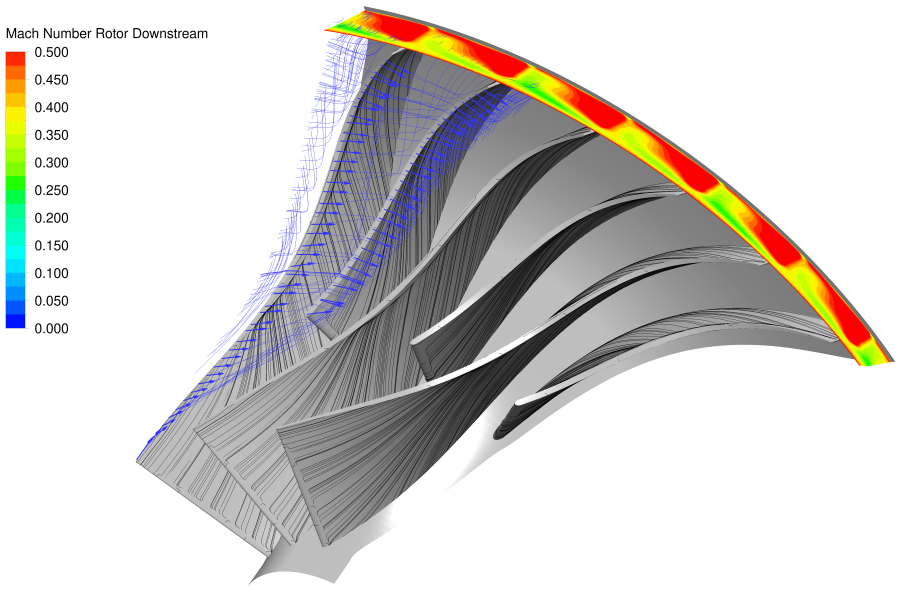

Figure 4.6: Streamlines on blades (black) and from tip clearance (blue), combined with Mach number contour downstream of the rotor.

4.1.4 Impeller Exit Flow Profile

Figure 4.7 shows the normalised circumferential and radial velocities at the impeller exit in the vaneless space, where the velocities are normalised by the blade speed, U_2. In the radial direction, wakes from the impeller blades are visible, along with a low-momentum zone near the shroud, discussed in Sec. 2.1.1. This corresponds to the low-momentum tip flow from the impeller and the reversed flow indicated in the swirl angle in Fig. 4.9. On the pressure side of the impeller blades, a high-momentum region can be observed. The circumferential velocity also exhibits regions of both low and high momentum; however, these are not clearly divided between the pressure and suction sides, but instead vary both circumferentially and radially (from hub to shroud)

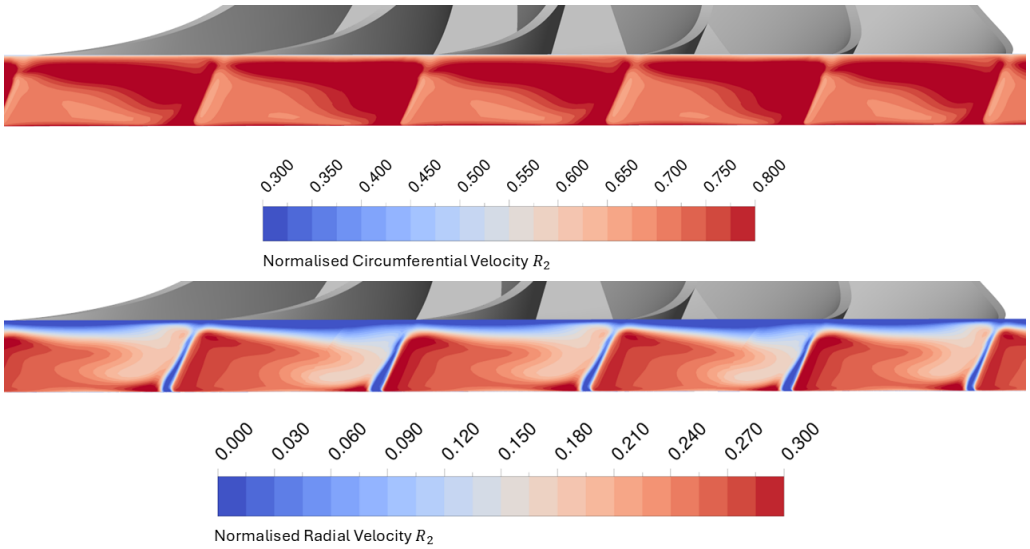

Figure 4.7: Normalised circumferential and radial velocity at the impeller exit, R_2.

The low momentum flow in the radial direction at the shroud is seen also at 105% of impeller exit radius in Fig. 4.8. Here the contours have been averaged downstream of the stage mixing-plane interface which mixes out the flow features but the trend is still seen. The diffusion can be observed by the lighter contour colours seen at 110% and 120% which is found in App. B.

Figure 4.9 illustrates the swirl angle and absolute Mach number at four different radial positions in the vaneless space. The swirl angle remains almost constant at all blade spans except for at the tip and the hub at approximately 72.5°, as expected in a vaneless space (Sec. 2.2.1). With the increase in radius the frictional losses increase at both the hub and the tip leading to a decrease in the meridional velocity and consequently increasing the swirl angle. At the tip due to the presence of a pinch the is a local acceleration of the flow to impart momentum to the low momentum flow from the tip region. The absolute Mach number illustrate a more uniform profile and decreasing in magnitude in the radial direction. Right after the impeller exit the flow is transonic.

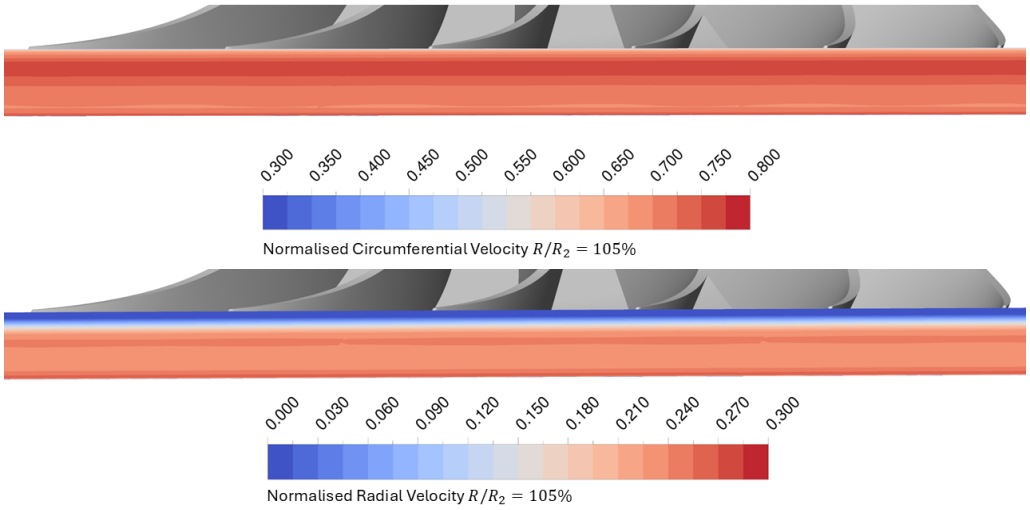

Figure 4.8: Normalised circumferential and radial velocity at 105% of the impeller exit, $R/R_2 = 105\%$.

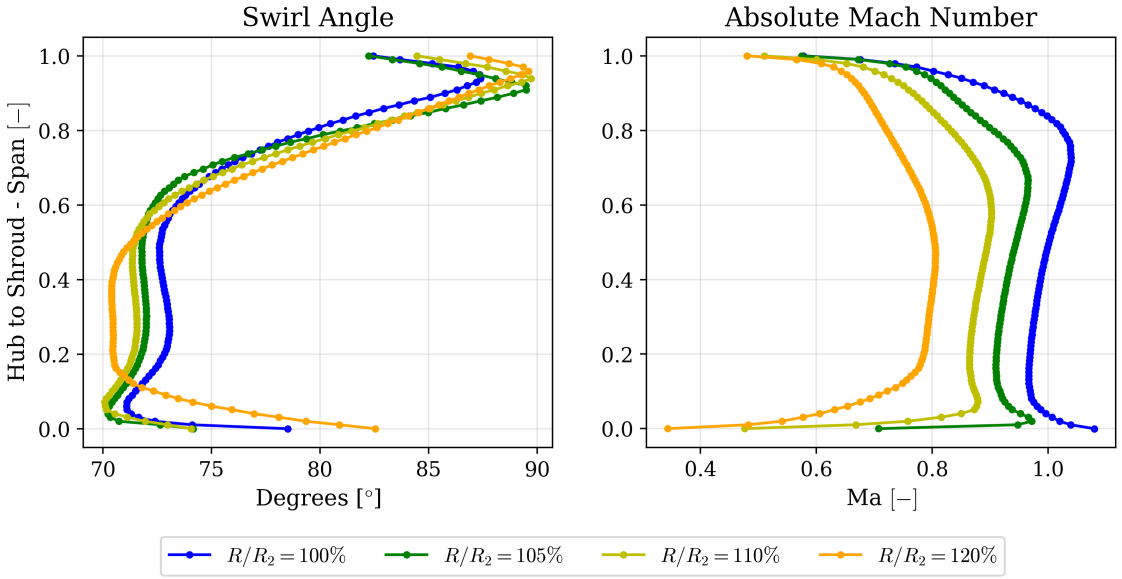

Figure 4.9: Swirl angle (left) and Mach number (right) at different radial positions.

4.1.5 100% Speedline Comparison

Figure 4.10 show a speedline at 100% rotational speed for PRTT and isentropic efficiency. Like in the mesh study and turbulence model comparison there is an overprediction at the design mass flow rate. This overprediction increases closer to stall and decreases and eventually becomes an underprediction closer to choke.

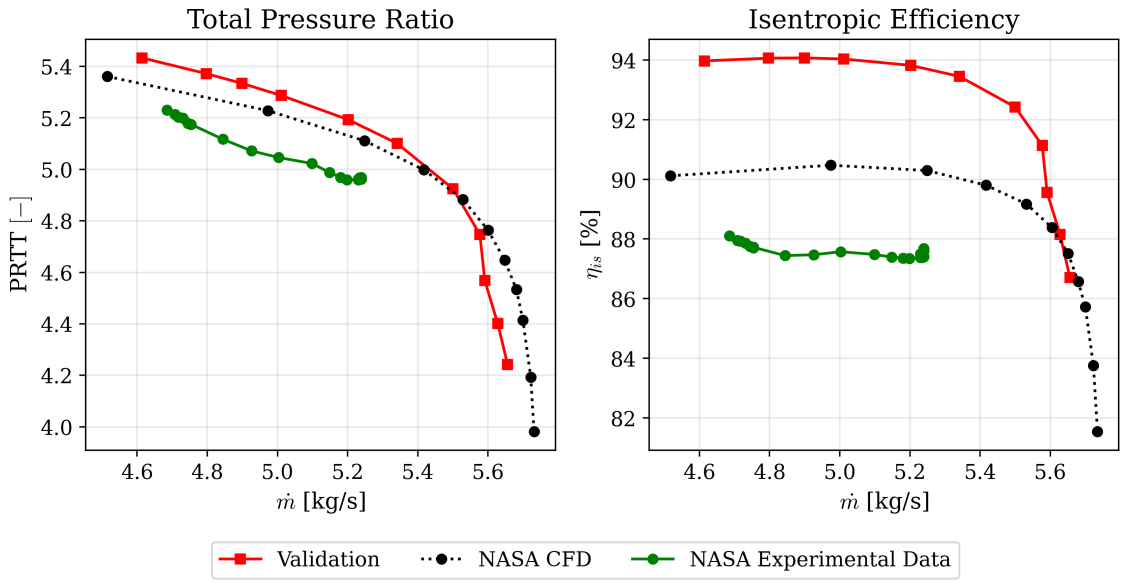

Figure 4.10: Total pressure ratio (left) and isentropic efficiency (right) vs inlet mass flow.

The 100% speedline presented in this thesis work is seen to move to lower massflows compared to those presented by NASA, i.e., the choking massflow is lower compared to NASA by 1.31%. In contrast, the massflow at which stall occurs is 1.89% higher compared to that predicted by NASA.

This difference in the operational range and choking mass flow indicates that the throat area of the two geometries are not identical. The lower choking massflow indicates that the throat area of the geometry used for this thesis work is lower compared to the geometry numerically evaluated by NASA. A smaller throat also allows for higher pressure rise which is observed as the general behaviour over a majority of the range. The uncertainty in throat can be attributed to:

- Uncertainty in the LE shape which directly affects the throat area.
- The assumption of the thickness distribution of both the main and splitter blade, which affects the throat area and can lead to both the position of the throat area and the value of throat area to change at all spans.
- Uncertainty in the LE shape also affects the incidence angle, position and strength of the suction peak, which in turn can lead to separations especially at higher spans where the relative inlet Mach number is high which in turn can lead to shock induced separations.

The uncertainty in the value of the throat area and LE geometry is therefore considered to be the main contributor to the observed performance differences in the speedlines. Additional sources of uncertainty may arise from the digitisation of blade angle and thickness distributions, as these were extracted from graphical data rather than tabulated values. While modern resolution improves accuracy, discrepancies compared to the original data are unavoidable. Additionally, differences in the numerical setup used by NASA and in this thesis work can be considered an additional source of uncertainty.

4.2 Diffuser Study

CFD data from NASA for diffuser performance (C_P and ζ) is only available as averaged values from discrete points in the simulations, intended to correspond to probe locations in the experimental setup. For the diffuser, these positions are located at the diffuser LE and the OGV LE (downstream of radial to axial bend). Since the present simulations do not include the radial-to-axial bend, this data is not directly comparable. The kinetic energy recovery coefficient (ξ) is not provided, as it is defined such that the three parameters sum to unity. Numerical data such as efficiency and pressure ratio is available as area-averaged quantities over the impeller-diffuser stage.

4.2.1 Vaneless and Vaned Diffuser comparison

Here a comparison is made between the vaneless diffuser case and the wedge vaned diffuser case, labelled as WD. First a comparison is made of the overall diffuser performance parameters, C_p, ζ and $\eta_{is,stage}$ as illustrated in Fig. 4.11. The overall C_P is seen to go up from 0.285 for the vaneless case to 0.689 for the wedge vaned diffuser case. As a result of the increased wetted surface for the vaned diffuser case, the total pressure losses also marginally increase for the wedge vaned case in comparison to the vaneless case. The increase in ζ leads to a corresponding drop in efficiency.

Additionally, the vaned diffuser allows for de-swirling of the flow compared to a vaneless diffuser which maintains a nearly constant swirl angle from the diffuser inlet to outlet except for blade spans close the hub and the tip region (Fig. 4.9). The hub-to-shroud profiles for the swirl angle and the absolute Mach number at different radial positions through the vaned diffuser is presented in Fig. 4.12. The flow angle exiting the diffuser is close to the exit blade metal angle of the diffuser of 58 degrees except at blade spans below 20%. Here it is observed that while the absolute Mach number of the flow is significantly reduced, a large swirl component of the flow still remains, which must be removed before the flow is allowed into the combustor.

The significant increase in diffuser performance with the addition of vanes, in ad-

dition to the large amount of swirl remaining in the flow at the exit of the diffuser clearly motivates the need to have vaned diffusers for such applications where there is limited space available to achieve the required flow diffusion.

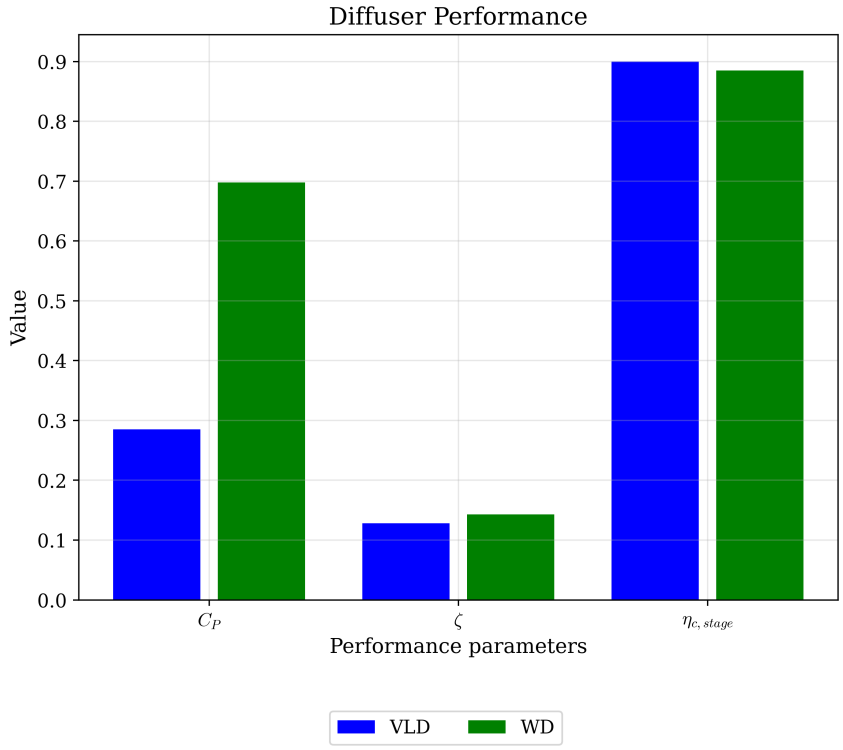

Figure 4.11: Diffuser performance parameters for the VLD and WD.

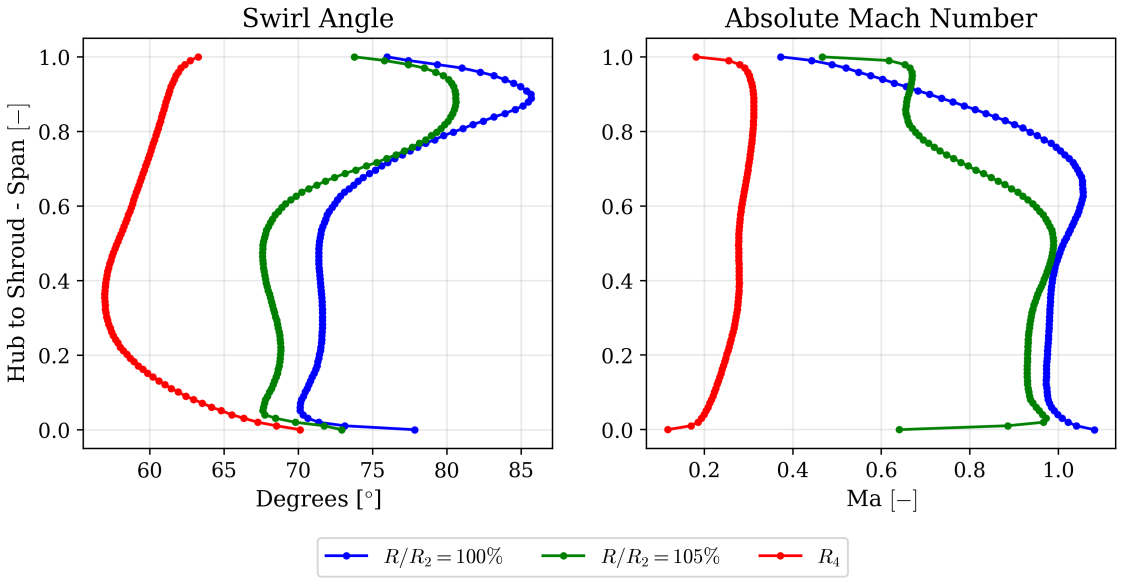

Figure 4.12: Swirl angle (left) and Mach number (right) at different radial positions for the vaned base diffuser, WD.

4.2.2 Performance at ADP

The previous section clearly illustrates the need to include diffuser vanes in applications which have limited radial space available to diffuse the flow. This section further investigates different types of vaned diffusers; namely the wedge diffuser (WD), the wedge splitter diffuser(WSD), cascade diffuser (CD), and cascade splitter diffuser (CSD). Table 4.4 presents the performance parameters for the investigated vaned diffuser configurations at ADP. Of the four diffusers investigated, the cascade diffuser yields the highest pressure recovery coefficient with a C_P of 0.712 while the lowest total pressure loss coefficient is observed with the wedged diffuser with splitters with a ζ of 0.141. Compared to the WD, the WSD shows a decrease in C_P from 0.698 to 0.684 respectively. A reduction in ζ from 0.143 to 0.141 for the WSD is seen.

Similar trends are observed when introducing a splitter vane in the cascade vane design, i.e., going from CD to CSD. However, for these configurations, ζ increases instead from 0.161 to 0.165, and the other changes are more pronounced, including a larger decrease in C_P and a greater increase in efficiency. Here it can be concluded that with the inclusion of splitter vanes a decrease is observed in the static pressure recovery coefficient. This decrease can be attributed to the decrease in the area ratio from diffuser inlet to outlet area as illustrated in Fig. 3.9. This conclusion is further supported by the first term of the Lieblein diffusion factor (DF_1) in Tab. 4.4. The first term in Lieblein diffusion factor is a measure of the flow diffusion (1-c_4/c_3). The velocity ratio (c_4/c_3) is inversely proportional to the area ratio through the diffuser vanes (A_3/A_4). This conclusion is further supported by the de Haller number which is higher for both WSD compared to WD and CSD compared to CD. The de Haller number is a direct measure of the flow diffusion through the diffuser vanes. Finally it is seen that the flow turning term (DF_2) in Tab. 4.4 is constant through all four diffuser designs as a result of having constant inlet and outlet blade metal angles for all four investigated diffusers.

Table 4.4: Summary of the performance parameters for all vaned diffusers in the ADP.

Name	C_P [−]	ζ [−]	η_{is} [%]	DF_1	DF_2	DH
WD	0.698	0.143	88.492	0.67	0.20	0.33
WSD	0.684	0.141	88.554	0.66	0.20	0.34
CD	0.712	0.161	87.918	0.67	0.20	0.33
CSD	0.650	0.165	88.361	0.65	0.20	0.35

4.2.3 Flow Field at ADP

A much larger wake is observed from the TE of WD compared to the wake from the TE of the CD as seen in Fig. 4.13 and Fig. 4.14. As previously stated, in aero-

engine applications, where the flow must be turned from radial to axial direction, vane trailing-edge geometries are particularly important. A rounded TE is generally preferred over wedge-shaped designs, as the latter tend to generate large wakes. Within the radial-to-axial bend, the pressure gradient ($\partial p/\partial r > 0$) is stronger near the shroud, causing wake structures to migrate toward the hub. This requires additional axial distance for flow reattachment before the LE of the axial OGV, which is often limited in compact aero-engine configurations. Additionally, since no significant diffuser performance benefits are observed for the WD and WSD cases compared to the CD and CSD cases as observed in Tab. 4.4, the remaining analysis is conducted for the cascade airfoil diffusers (CD and CSD).

When introducing splitter vanes for the cascade diffuser, an additional separation is observed on the pressure side of the main vane. This separation is a suspected to be a consequence of an unequal flow distribution on the two sides of the splitters vanes as a result of an unequal area ratio on the two sides of the splitter vanes. Since the flow coming in to the splitter vanes is not uniform it follows that there exist an unequal massflow distribution through the two splitter passages. Even though the splitter is placed circumferentially midway between to main vanes, as a function of the blade angle distribution the exit areas are not necessarily identical. Typical ways to address this unequal flow through the two splitter blade passages is to adjust either the circumferential position of the splitter vane or to adjust its lean angle.

The streamlines on the CSD vanes and splitters are shown in Fig. 4.16. These confirm the presence of separation on the pressure side of the main vane, forming a circulation pattern. A corner separation close to the shroud is also visible. In Appendix D, the span-wise distributions at 25 and 75% spans show that the incidence angle is higher at 75% span, as illustrated in Fig. D.4. This corresponds to the swirl distributions observed in Figures 4.9 and 4.12, where higher swirl levels are present towards the shroud. This coincides with the location of the observed corner separation.

4.2.4 100% Speedline for All Diffusers

Figure 4.17 illustrates the speedline at 100% speed of PRTT and isentropic efficiency for all investigated diffusers. There is a shift in the operating line at choke from 5.6 kg/s to 5.5 kg/s from the wedge diffusers to cascade diffuser with splitter. This shift is proportional to the small decrease of the throat area (Sec. 3.4). The aerodynamic effect of the higher area ratio of the cascade airfoil diffuser without splitter vanes (CD) compared to remaining three cases is observed in the extreme short operating range compared to the other three cases.

The best speedline characteristic is observed for the CSD case as a results of the smooth onset of stall with no sharp decrease in isentropic efficiency, as observed for the rest of the cases. In Fig. 4.18, the speedlines for C_P and ζ are shown for all diffusers. Here it is concluded that while no significant benefit is observed in the diffusion performance parameters (C_P and ζ) while introducing splitter vanes for a cascade airfoil, large benefits are observed in the operational range of the

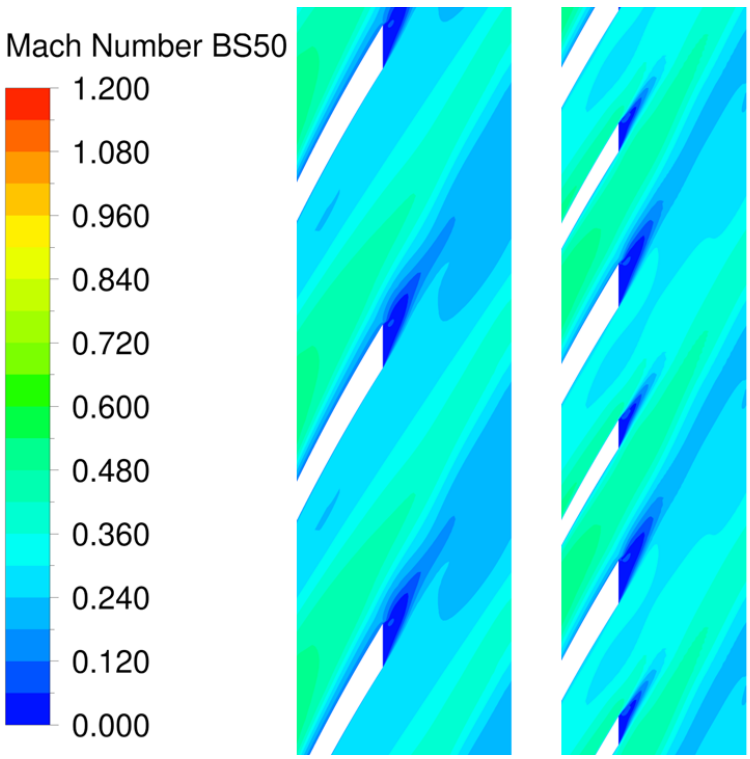

Figure 4.13: Wake from the TE of WD (left) and WSD (Right), seen at 50% blade span.

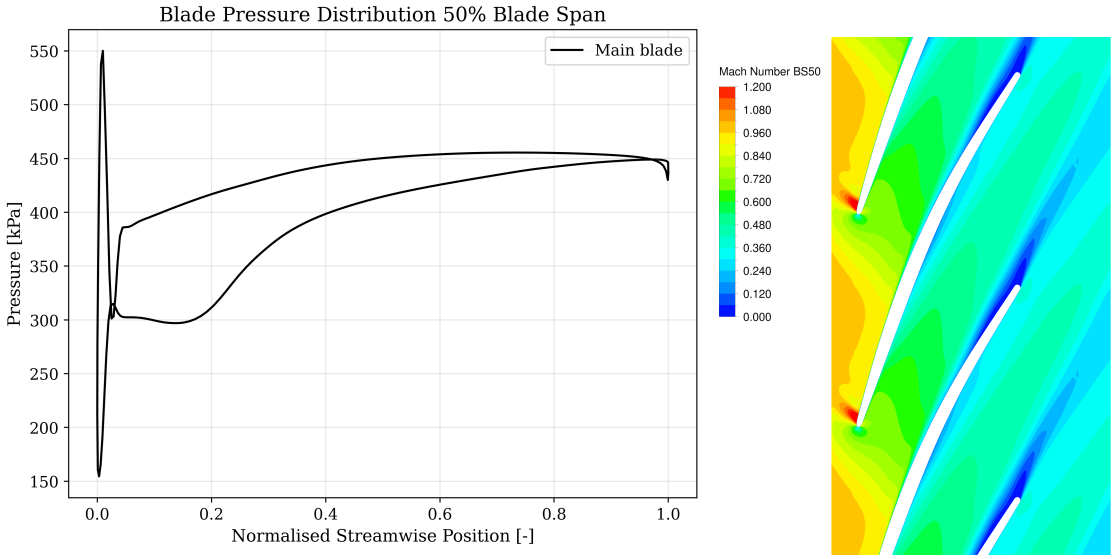

Figure 4.14: Mach Number contour at 50% blade span of CD, in the ADP.

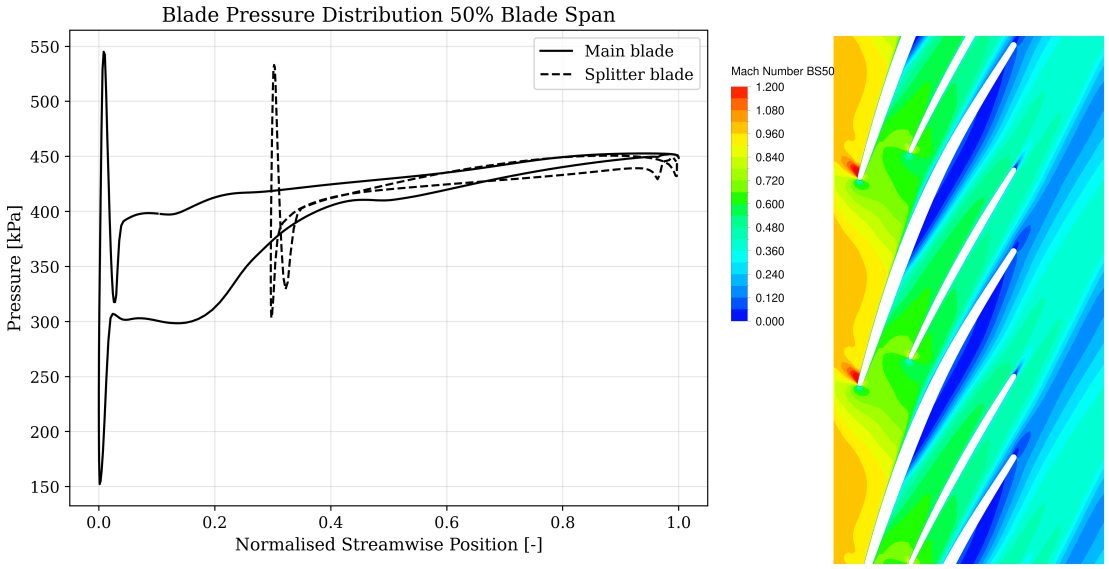

Figure 4.15: Mach Number contour at 50% blade span of CSD, in the ADP.

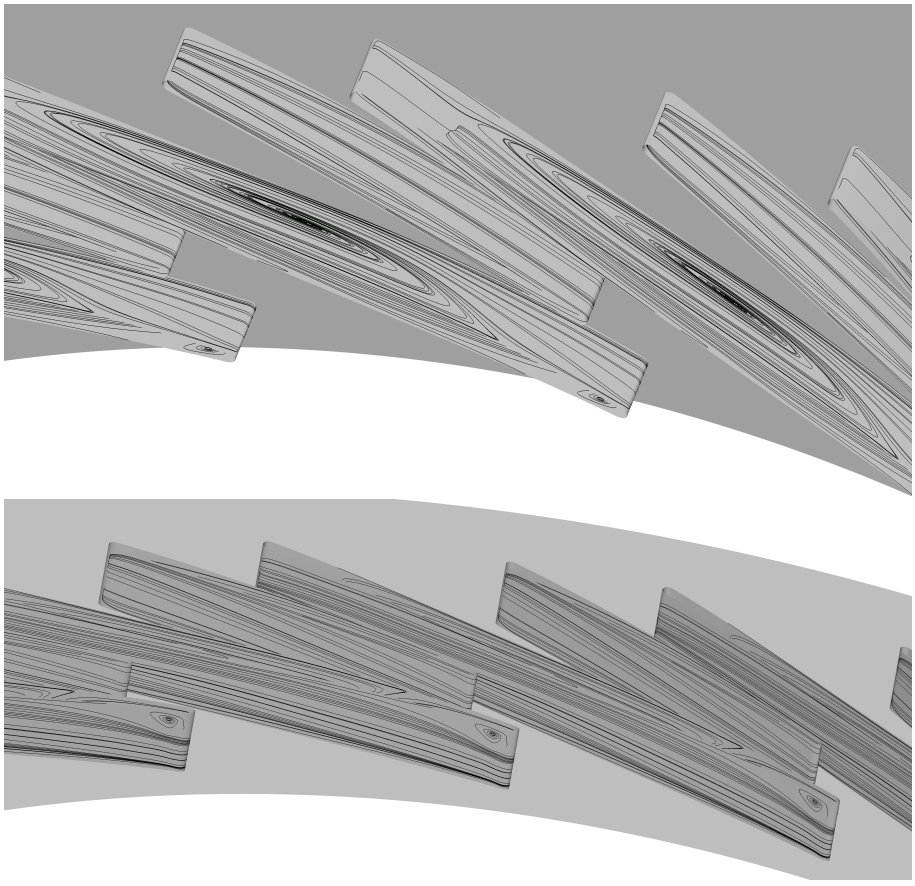

Figure 4.16: Streamlines of the separation on the pressure side of the main vane (top) and streamlines of the suction side (bottom) with the corner separation at the shroud, both of the CSD.

impeller-diffuser stage.

Lastly, a comparison is made between the impeller-diffuser performance for the cascade airfoil with splitters (CSD) to the NASA HECC impeller-diffuser numerical data in Fig. 4.19. This figure illustrates a smaller loss in choke margin for the CSD presented in this thesis compared to the diffuser design used by NASA HECC, i.e., the throat area matching for the CSD design presented in this thesis is an improvement over the NASA HECC design. Here it is also noted that at the ADP, the PRTT achieved by the CSD design presented in this thesis closely matches the NASA HECC design. The isentropic efficiency of the CSD design presented in this thesis is higher by 1.5% than the NASA HECC design. However, the CSD design seem to stall at a massflow rate of 4.8 kg/s compared to 4.6 kg/s for the NASA HECC design.

Therefore it is concluded that the CSD design meets the initial thesis target to design a diffuser with the same radius ratio R_4/R_2 as the NASA HECC diffuser and achieve an equal or similar performance to the NASA HECC.

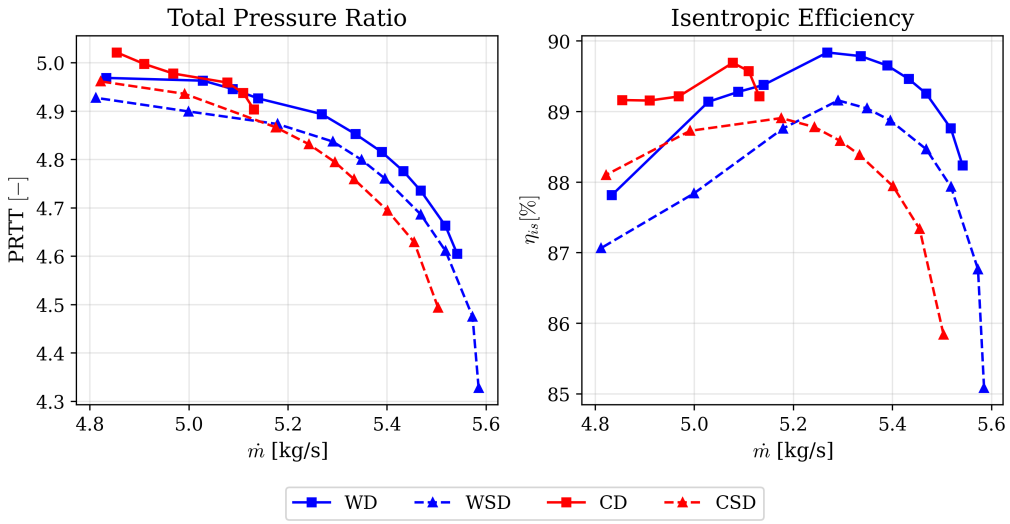

Figure 4.17: Total pressure ratio and isentropic efficiency for the stage of all diffusers, at 100% rotational speed, compared with NASA's CFD results.

4.3 Splitter Lean and Circumferential Shifting

As mentioned in Sec. 4.2.3 the massflow rate is believed to be unequal between the two the splitter vane passages. This section presents simulations of the CSD design with different lean angles on the splitter vane and circumferentially shifting the splitter vane to the pressure side of the main vane done at ADP. Figure 4.20 illustrates the summarised results in terms of C_P and ζ. The labels in Fig. 4.20 stand as L for Lean and the number for degrees of lean, i.e., 1°, 2°, 3°. PS stands for Pressure Side and the number corresponds to 2.5 percent shift towards the pressure side of the main blade, i.e., 2.5, 5.0 and 7.5%. An increase in C_P and decrease in ζ

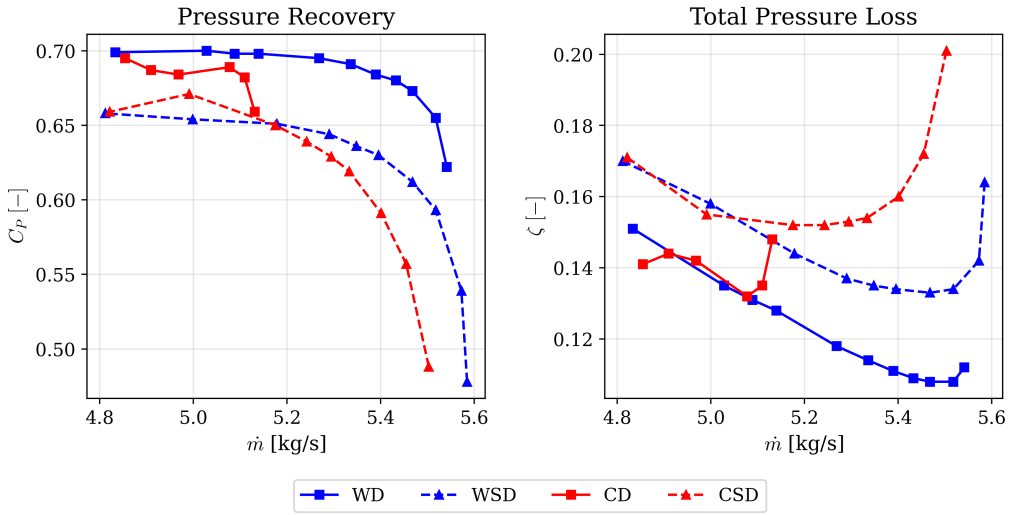

Figure 4.18: Pressure recovery and total pressure loss coefficients of the diffusers, at 100% rotational speed.

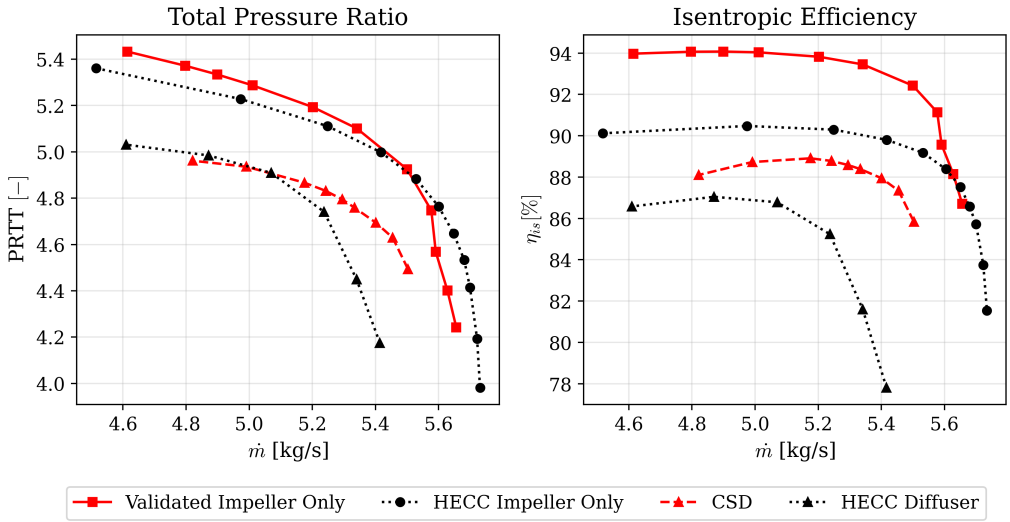

Figure 4.19: Total pressure ratio and isentropic efficiency for the stage with CSD and impeller only, at 100% rotational speed.

is seen both with the increasing lean angle on the splitter vane and the shift of the splitter vane towards the pressure side. It can be observed that the splitter vane with 3° lean (CSDL3) achieves the highest C_P pf 0.664 and lowest ζ of 0.157. A speedline at 100% speed is shown in Fig. 4.21 comparing the C_P of the CSD and CSDL3. Here it can be observed that the implementing the lean increase the instability and decrease the operating range. It can be concluded that adding this amount lean to the splitter vanes is not a viable option for the cascade diffuser. However, it shall not be concluded that this effect seen, is equal for all lean and shift options.

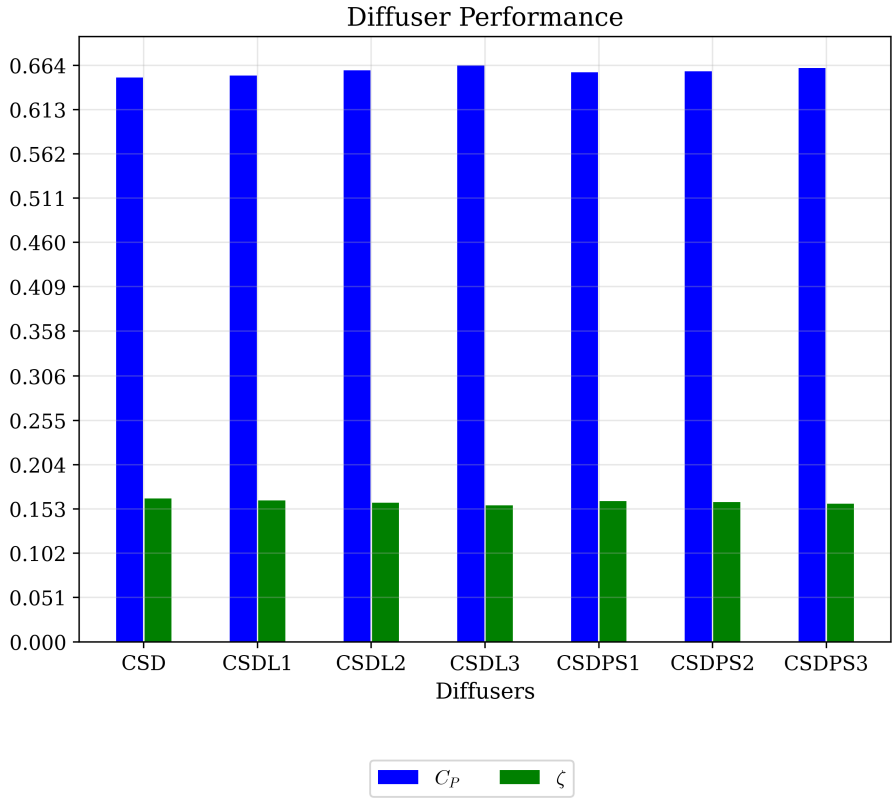

Figure 4.20: Results of leaning and shifting the splitter vane towards pressure side of the main vane, at ADP.

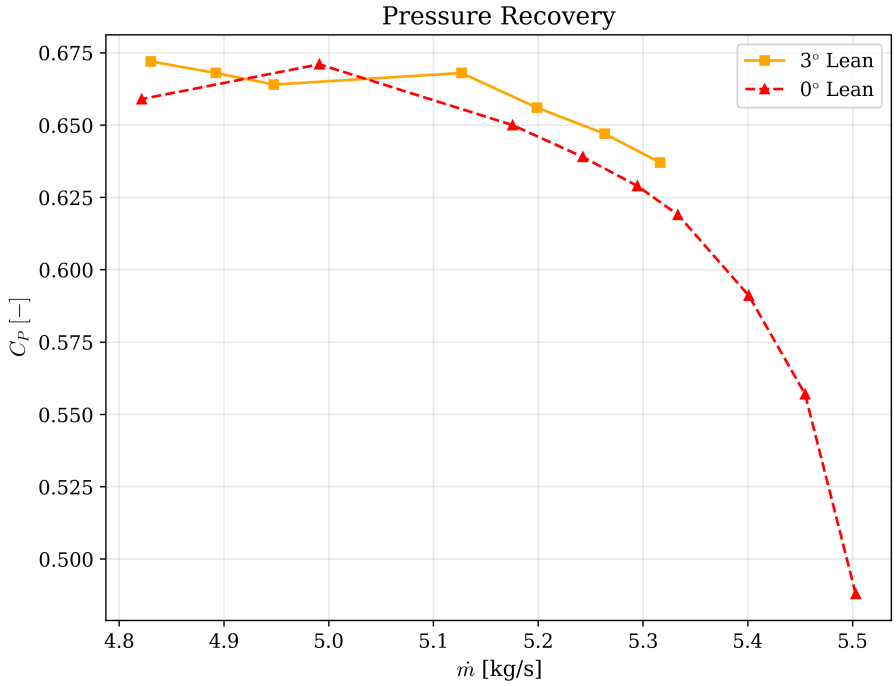

Figure 4.21: Speedline comparison of PRTT and isentropic efficiency for the CSD with no lean and 3° lean on the splitter vanes.

5

Conclusions

This thesis has investigated the aerodynamic performance of centrifugal compressor diffusers for small aero-engine applications using a validated NASA HECC impeller as a baseline. The main conclusions drawn from the results and discussion are summarized below.

- A replicated geometry of the NASA HECC impeller was successfully generated using publicly available data and demonstrated reasonable agreement with NASA CFD results.
- Differences in predicted choke mass flow and operating range compared to NASA results indicate discrepancies in the effective throat area of the replicated geometry.
- The impeller exit flow is highly non-uniform, characterised by strong swirl, tip-clearance-induced low-momentum regions, and transonic flow conditions, which strongly influence diffuser design.
- The inclusion of vanes significantly improves pressure recovery compared to a vaneless diffuser, confirming that vaned diffusers are necessary for compact aero-engine applications.
- The wedge diffuser (WD) provides good pressure recovery but generates strong trailing-edge wakes, which are detrimental for downstream flow uniformity. The cascade diffuser (CD) achieves the highest pressure recovery at ADP but exhibits poor stability and a limited operating range.
- The introduction of splitter vanes:
  - Improves flow stability and extends the operating range.
  - Reduces peak pressure recovery due to decreased effective area ratio and increased blockage.
- Leaning and circumferential shifting of splitter vanes can improve pressure recovery and reduce losses at the design point. However, these modifications negatively affect stability and reduce the operating range. As a result, splitter lean is not considered a viable design strategy for improving overall diffuser performance in this configuration.

- The initial objective of achieving equal performance at the same radius ratio as the NASA HECC diffuser is partially met. The cascade diffuser with splitter vanes (CSD) demonstrates comparable performance to the reference design while improving operating characteristics such as stability and choke behaviour.

The results provide valuable insights into diffuser design trade-offs and confirm that careful control of vane geometry, splitter configuration, and flow distribution is essential for high-performance small aero-engine applications. The study highlights the importance of balancing diffusion performance, flow stability, and downstream flow quality in the design of compact centrifugal compressor diffusers.

5.1 Future Work

The present study excludes the radial-to-axial bend and outlet guide vanes, which play a significant role in overall stage performance. Future work should include these components to fully assess the downstream impact of diffuser flow non-uniformities.

The results indicate that splitter vanes improve stability but introduce performance penalties. Further work could focus on optimizing splitter placement, and geometry to balance performance and stability more effectively.

Bibliography

[1] NASA Glenn Research Center, *The Brayton Cycle*, Accessed: Jan. 22, 2026. [Online]. Available: https://www.grc.nasa.gov/www/k-12/airplane/brayton.html

[2] S. L. Dixon and C. A. Hall, *Fluid Mechanics and Thermodynamics of Turbomachinery*, 7th ed. Boston: Butterworth-Heinemann, 2013, ISBN: 978-0-12-415954-9. DOI: 10.1016/C2011-0-05059-7

[3] PBS Group, *Small Aircraft Engines*, Accessed: Jan. 22, 2026. [Online]. Available: https://www.pbsaerospace.com/small-aircraft-engines

[4] E. Artetxe et al., 'Optimised methodology for aircraft engine IBRs five-axis machining process,' *International Journal of Mechatronics and Manufacturing Systems*, vol. 9, no. 4, pp. 385–401, 2016. DOI: 10.1504/IJMMS.2016.082873 eprint: https://www.inderscienceonline.com/doi/pdf/10.1504/IJMMS.2016.082873. [Online]. Available: https://www.inderscienceonline.com/doi/abs/10.1504/IJMMS.2016.082873

[5] G. Medic et al., 'High efficiency centrifugal compressor for rotorcraft applications,' National Aeronautics and Space Administration, Tech. Rep. NASA/CR-2014-218114/REV1, 2017, Accessed: Feb. 15, 2026. [Online]. Available: https://ntrs.nasa.gov/citations/20180001471

[6] N. Cumpsty, 'The Diffuser of the Centrifugal Compressor,' in *Compressor Aerodynamics*, Essex, England: Longman Scientific and Technical, 1989, ch. 7, pp. 266–301.

[7] R. C. Dean Jr and Y. Senoo, 'Rotating wakes in vaneless diffusers,' *Journal of Basic Engineering*, vol. 82, no. 3, pp. 563–570, Sep. 1960, ISSN: 0021-9223. DOI: 10.1115/1.3662659 eprint: https://asmedigitalcollection.asme.org/fluidsengineering/article-pdf/82/3/563/5762774/563_1.pdf. [Online]. Available: https://doi.org/10.1115/1.3662659

[8] R. V. d. Braembussche, *Design and Analysis of Centrifugal Compressors*. John Wiley & Sons, 2019, ISBN: 978-1-11942-4-093. [Online]. Available: https://app.knovel.com/hotlink/toc/id:kpDACC000C/design-analysis-centrifugal/design-analysis-centrifugal

[9] M. Schleer and R. S. Abhari, 'Clearance effects on the evolution of the flow in the vaneless diffuser of a centrifugal compressor at part load condition,' *Journal of Turbomachinery*, vol. 130, no. 3, 2008, Cited by: 64. DOI: 10.1115/1.2776955 [Online]. Available: https://www.scopus.com/inward/record.uri?eid=2-s2.0-49049093100&doi=10.1115%2f1.2776955&partnerID=40&md5=8586e22b61cff8ac243cc934b6d19254

[10] M. Casey and C. Robinson, 'Diffuser Design,' in *Radial Flow Turbocompressors: Design, Analysis, and Applications*. Cambridge University Press, 2021, pp. 405–442.

[11] L. Reneau, J. Johnston and S. Kline, 'Performance and design of straight, two-dimensional diffusers,' *Journal of Fluids Engineering, Transactions of the ASME*, vol. 89, no. 1, pp. 141 –150, 1967, Cited by: 226. DOI: 10.1115/1.3609544 [Online]. Available: https://www.scopus.com/inward/record.uri?eid=2-s2.0-85008283168&doi=10.1115%2f1.3609544&partnerID=40&md5=41e158b84030aca91eb6ac70f15c3546

[12] S. Baghdadi and A. T. McDonald, 'Performance of three vaned radial diffusers with swirling transonic flow,' *Journal of Fluids Engineering*, vol. 97, no. 2, pp. 155–160, Jun. 1975, ISSN: 0098-2202. DOI: 10.1115/1.3447238 eprint: https://asmedigitalcollection.asme.org/fluidsengineering/article-pdf/97/2/155/5695842/155_1.pdf. [Online]. Available: https://doi.org/10.1115/1.3447238

[13] D. C. Wilcox, 'Formulation of the k-ω turbulence model revisited,' *AIAA Journal*, vol. 46, no. 11, pp. 2823 –2838, 2008, Cited by: 1171. DOI: 10.2514/1.36541 [Online]. Available: https://www.scopus.com/inward/record.uri?eid=2-s2.0-55749092935&doi=10.2514%2f1.36541&partnerID=40&md5=ac9817c5ea1476a743d10dba67bb03d9

[14] F. Menter, 'Two-equation eddy-viscosity turbulence models for engineering applications,' *AIAA Journal*, vol. 32, no. 8, pp. 1598 –1605, 1994, Cited by: 21492. DOI: 10.2514/3.12149 [Online]. Available: https://www.scopus.com/inward/record.uri?eid=2-s2.0-0028486598&doi=10.2514%2f3.12149&partnerID=40&md5=3a5e94756b3283ca6360ab12486bec2c

[15] H. M. I. Harrison, 'User's Guide for the NASA High Efficiency Centrifugal Compressor Data Archive,' NASA Glenn Research Center, Cleveland, Ohio,

Tech. Rep. NASA/TM-20240003692/REV1, 2024, Accessed: Mar. 2, 2026. [Online]. Available: https://ntrs.nasa.gov/citations/20250000831

[16] I. B. Celic, U. Ghia, P. J. Roache, C. J. Freitas, H. Coleman and P. E. Raad, 'Procedure for Estimation and Reporting of Uncertainty Due to Discretization in CFD Applications,' *Journal of Fluids Engineering*, vol. 130, no. 7, p. 078 001, Jul. 2008, ISSN: 0098-2202. DOI: 10.1115/1.2960953 eprint: https://asmedigitalcollection.asme.org/fluidsengineering/article-pdf/130/7/078001/5491455/078001_1.pdf. [Online]. Available: https://doi.org/10.1115/1.2960953

A

Impeller Mach Contours and BPD at 25 and 75% Blade Span

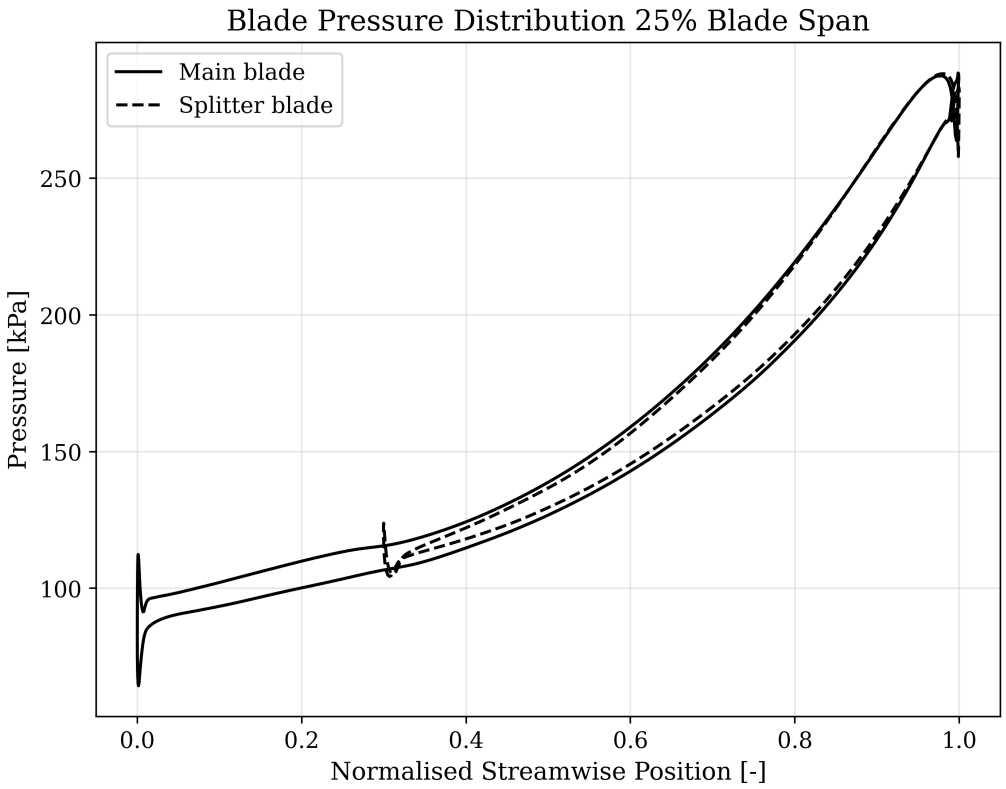

Figure A.1: Pressure distribution along the blades at 25% blade span.

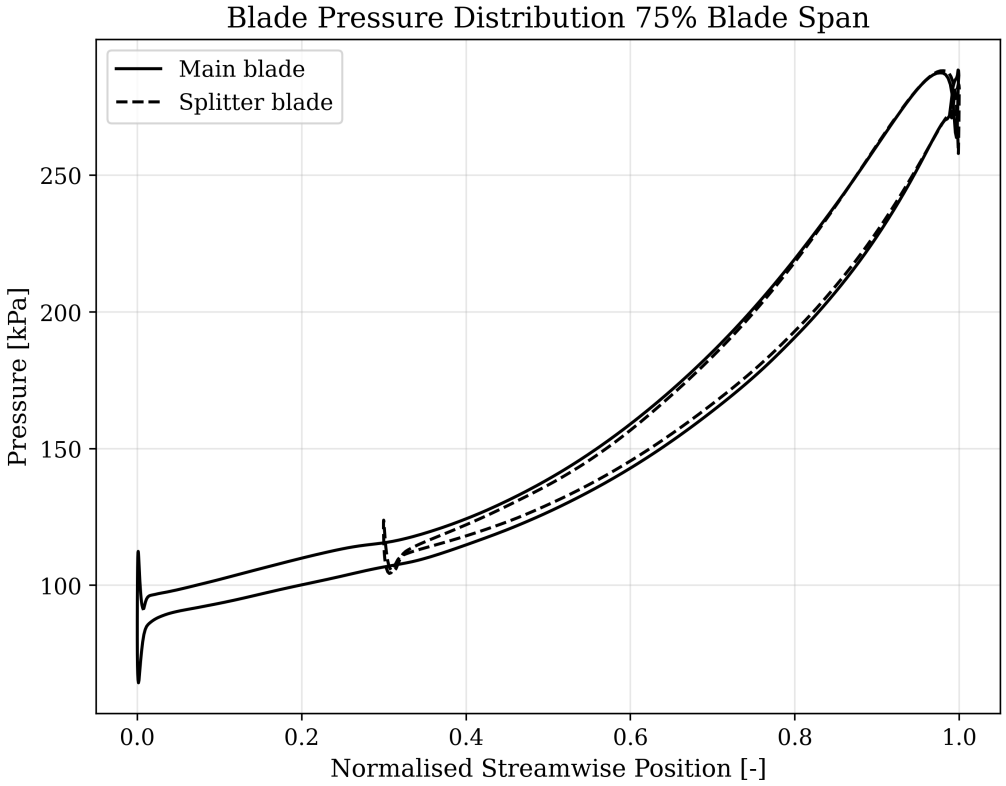

Figure A.2: Pressure distribution along the blades at 75% blade span.

B

Normalised Velocity Components at 110 and 120% of Impeller Exit Radius

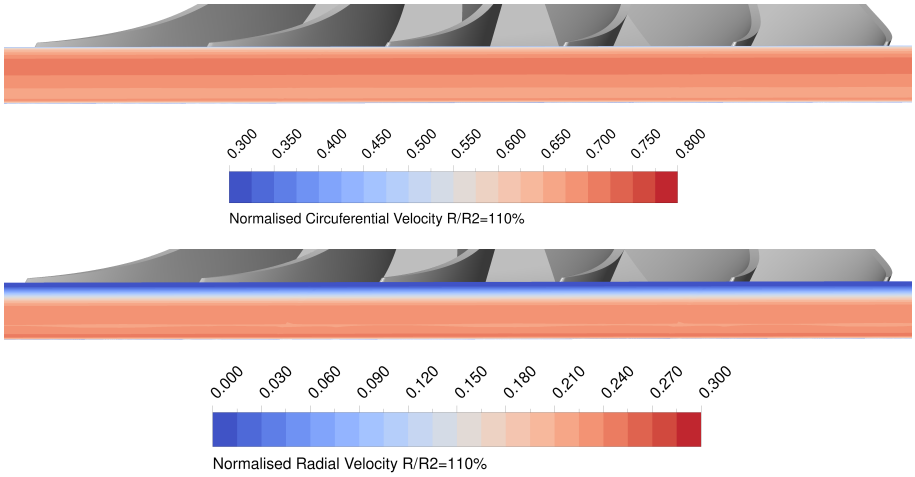

Figure B.1: Normalised circumferential and radial velocity at 105% of the impeller exit, $R/R_2 = 110\%$.

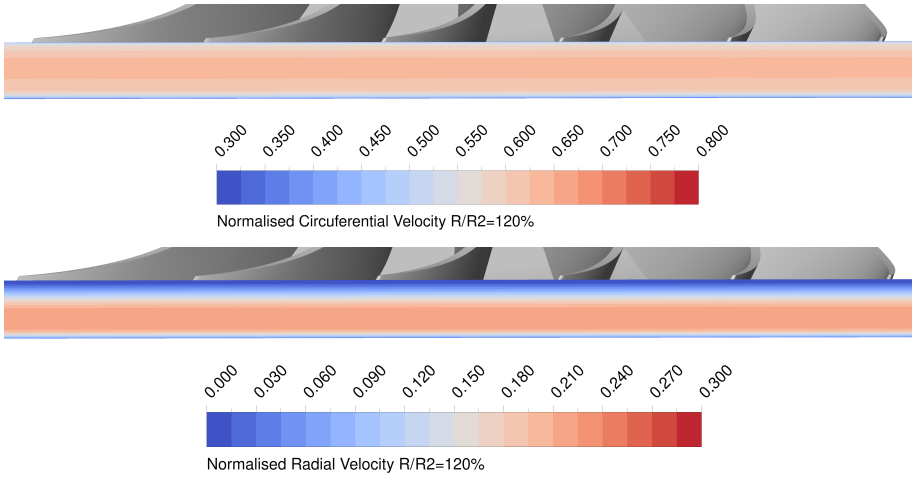

Figure B.2: Normalised circumferential and radial velocity at 105% of the impeller exit, $R/R_2 = 120\%$.

C

Wedged Diffusers Mach Contours and BPD at 25, 50 and 75% Blade Span

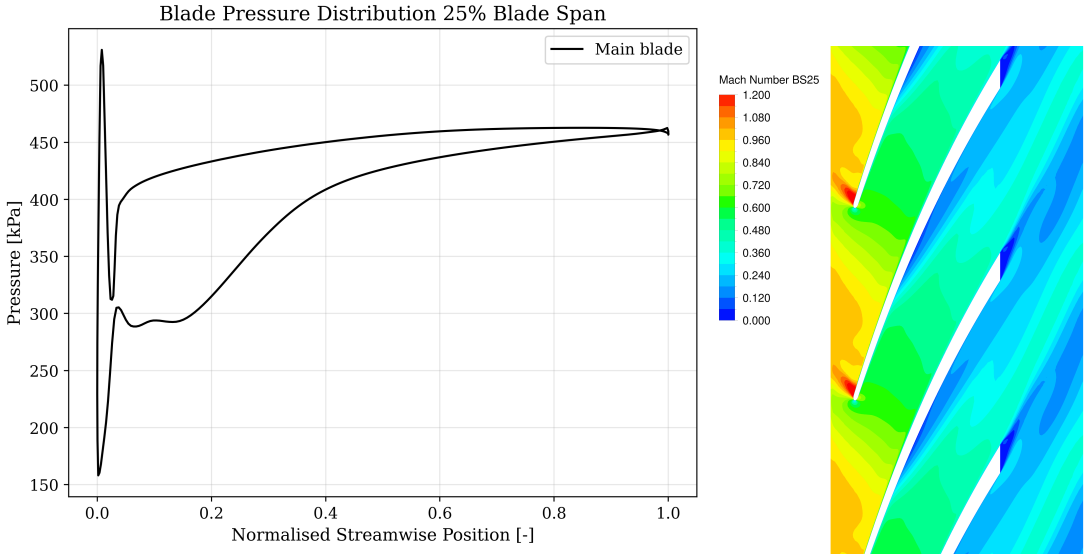

Figure C.1: BPD and Mach number contour at 25% blade span, WD.

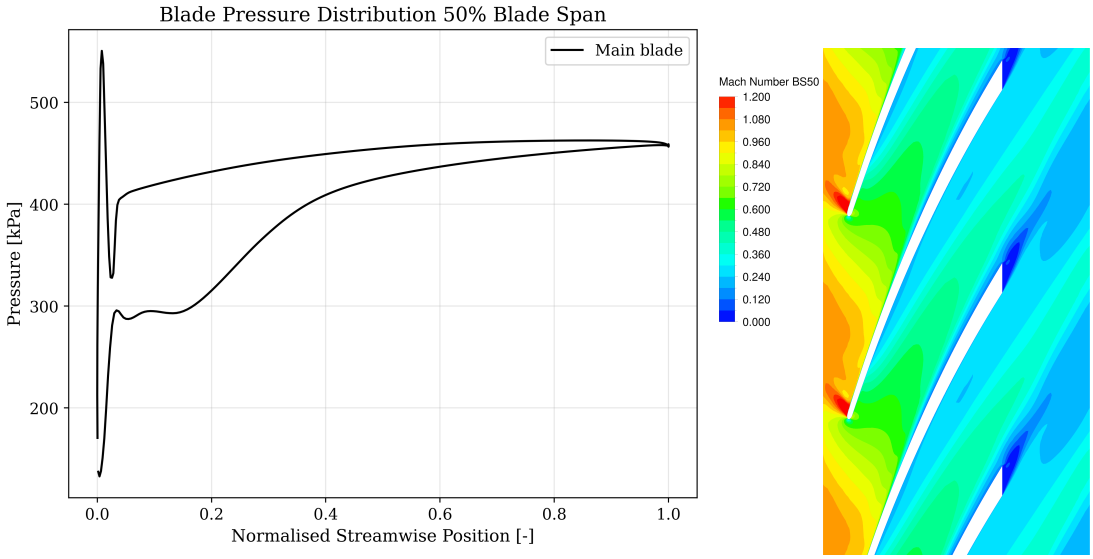

Figure C.2: BPD and Mach number contour at 50% blade span, WD.

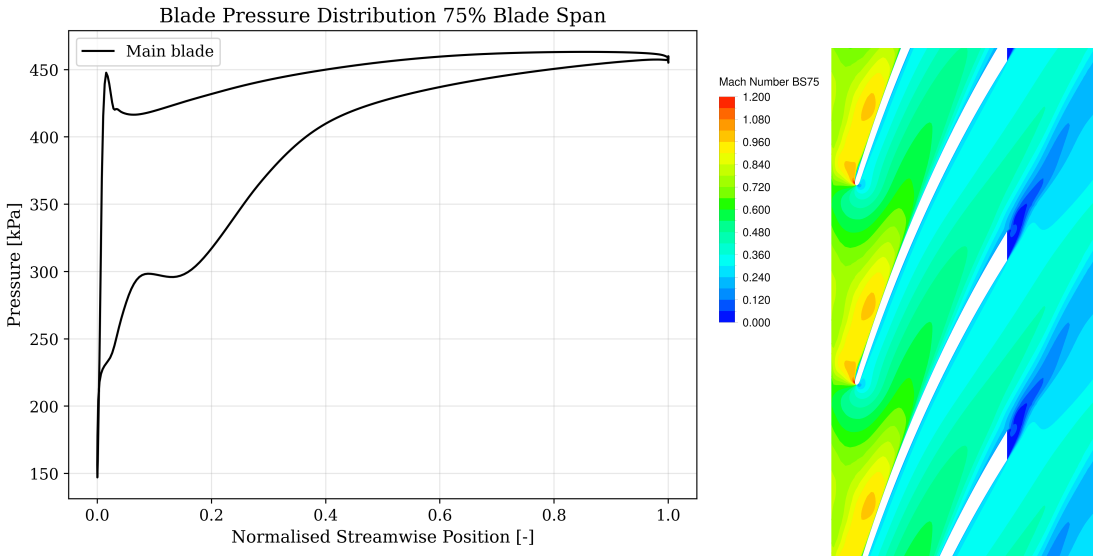

Figure C.3: BPD and Mach number contour at 75% blade span, WD.

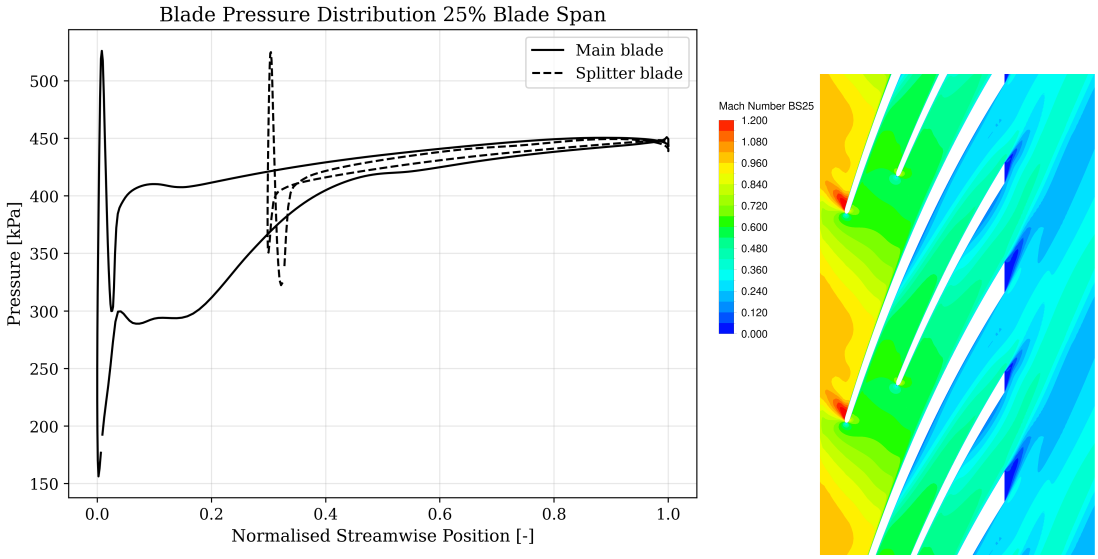

Figure C.4: BPD and Mach number contour at 25% blade span, WSD.

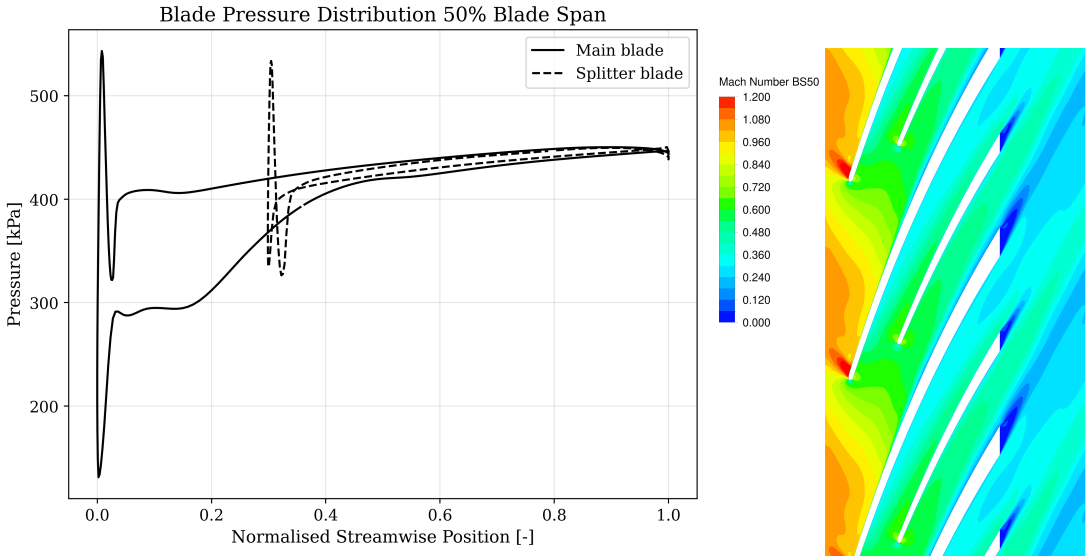

Figure C.5: BPD and Mach number contour at 50% blade span, WSD.

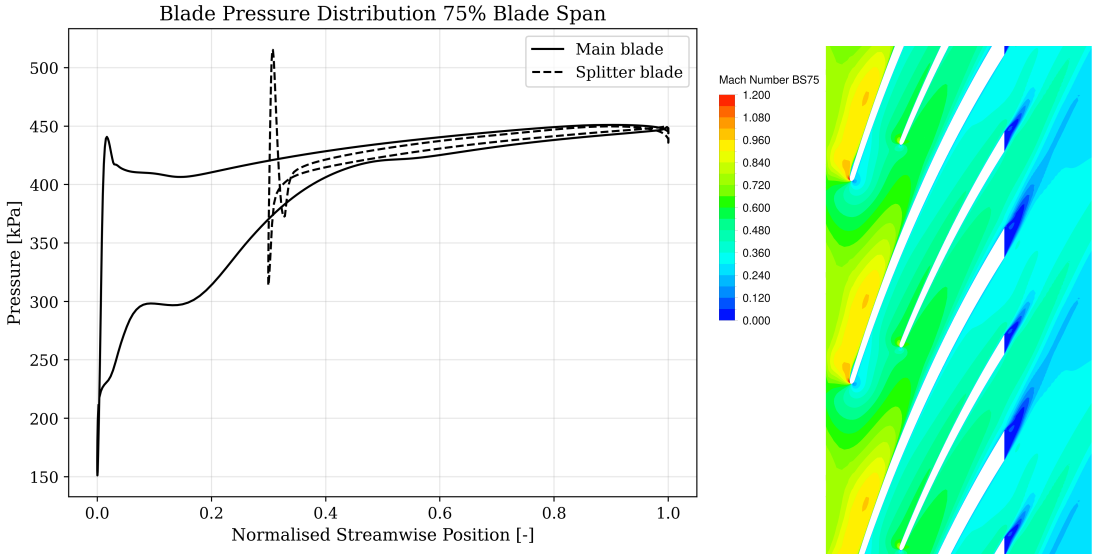

Figure C.6: BPD and Mach number contour at 75% blade span, WSD.

D

Cascade Diffusers Mach Contours and BPD at 25, 50 and 75% Blade Span

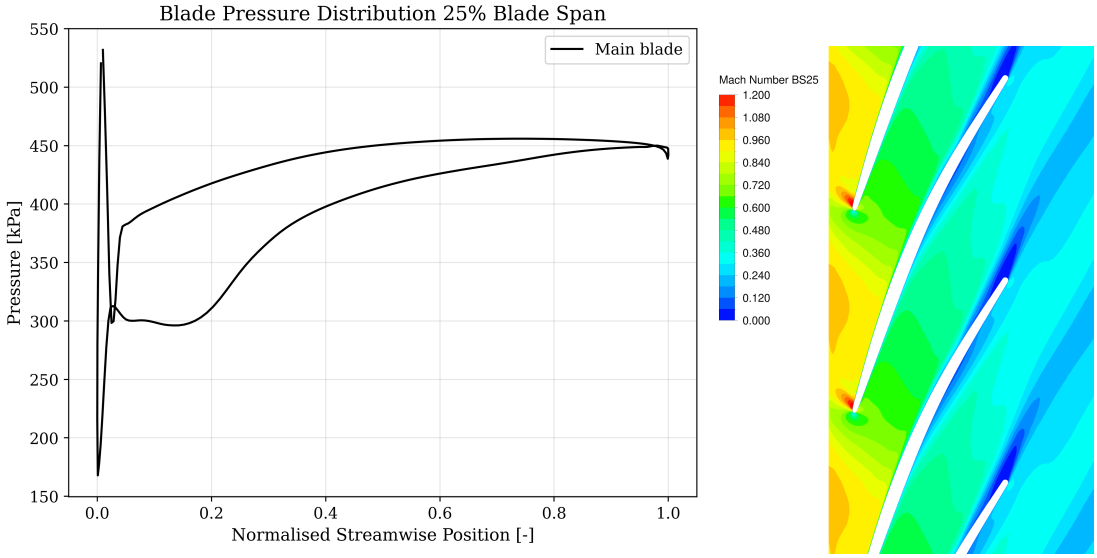

Figure D.1: BPD and Mach number contour at 25% blade span, CD.

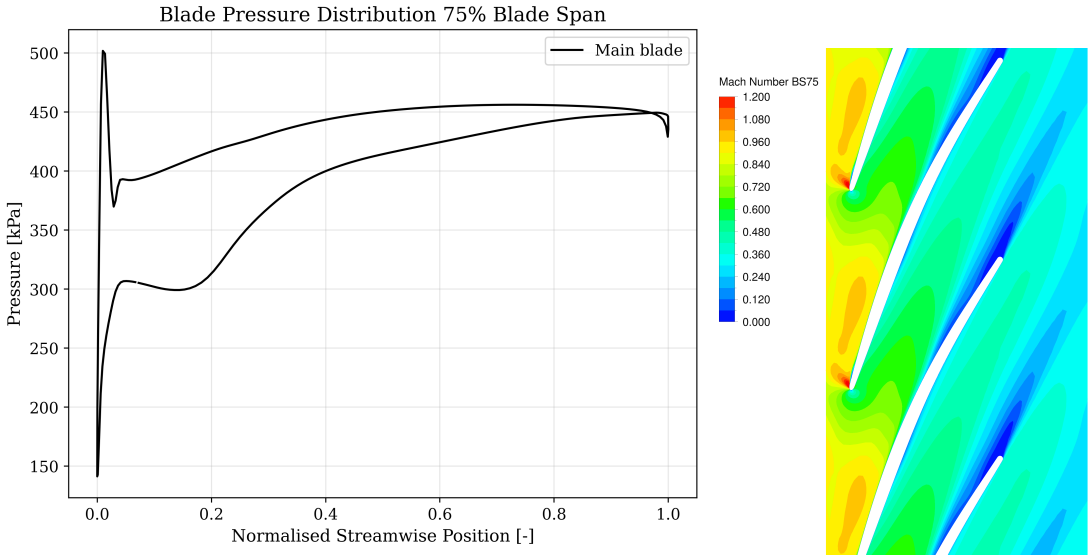

Figure D.2: BPD and Mach number contour at 75% blade span, CD.

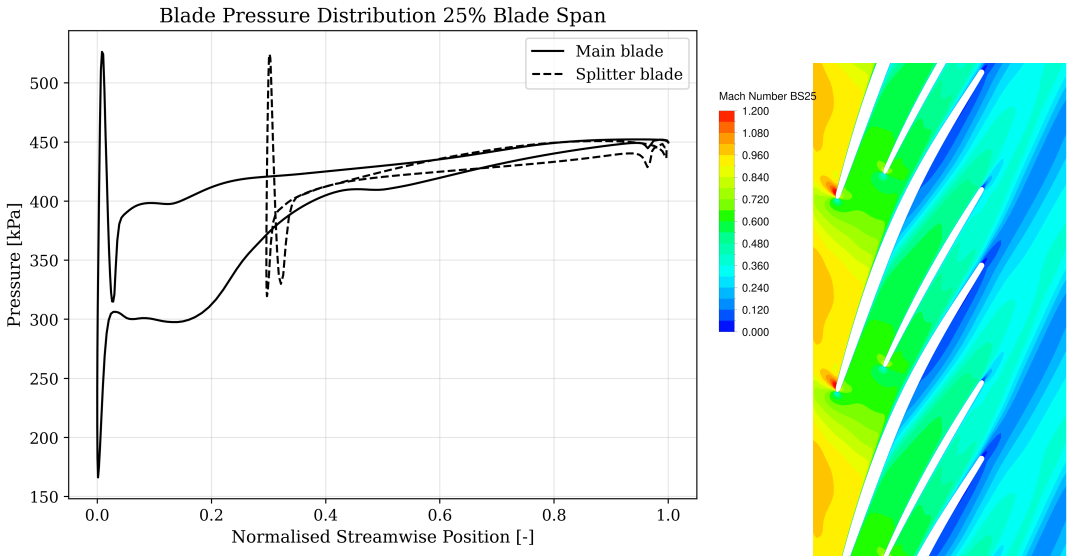

Figure D.3: BPD and Mach number contour at 25% blade span, CSD.

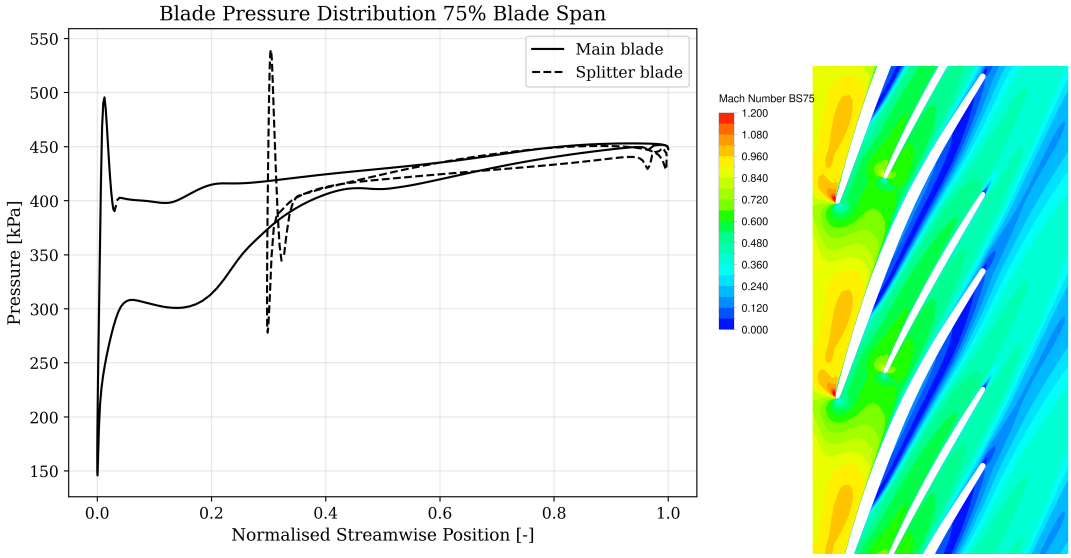

Figure D.4: BPD and Mach number contour at 75% blade span, CSD.

DEPARTMENT OF MECHANICS AND MARITIME SCIENCES
CHALMERS UNIVERSITY OF TECHNOLOGY
Gothenburg, Sweden 2026
www.chalmers.se

CHALMERS
UNIVERSITY OF TECHNOLOGY